Numerical Studies on Two-way Coupled Fluid Flow and Geomechanics in Hydrate Deposits

J. Kim, SPE; G. J. Moridis, SPE; Lawrence Berkeley National Laboratory; D. Yang, SPE, Texas A&M University; J. Rutqvist, SPE, Lawrence Berkeley National Laboratory

Abstract

Coupled flow and geomechanics play an important role in the analysis of gas hydrate reservoirs under production. The stiffness of the rock skeleton and the deformation of the reservoir, as well as porosity and permeability, are directly influenced by (and interrelated with) changes in pressure, temperature and fluid (water and gas) and solid (hydrate and ice) phase saturations. Fluid and solid phases may coexist, which, coupled with steep temperature and pressure gradients, result in strong nonlinearities in the coupled flow and mechanics processes, making the description of system behavior in dissociating hydrate deposits exceptionally complicated.

In previous studies, the geological stability of hydrate-bearing sediments was investigated using one-way coupled analysis, in which the changes in fluid properties affect mechanics within the gas hydrate reservoirs, but with no feedback from geomechanics to fluid flow. In this paper, we develop and test a rigorous two-way coupling between fluid flow and geomechanics, in which the solutions from mechanics are reflected in the solution of the flow problem through the adjustment of affected hydraulic properties. We employ the fixed-stress split method, which results in a convergent sequential implicit scheme.

In this study of several hydrate reservoir cases, we find noticeable differences between the results based on one- and two-way couplings. The nature of the elliptic boundary value problem of quasi-static mechanics results in instantaneous compaction or dilation over the domain, through loading from reservoir fluid production. This induces a pressure rise or drop at early times (low pressure diffusion), and consequently changes the effective stress instantaneously, possibly causing geological instability. Additionally, the pressure and temperature regime affects the various phase saturations, the rock stiffness, porosity, and permeability, thus affecting the fluid flow regime. These changes are not captured accurately by the simpler one-way coupling. The tightly coupled sequential approach we propose provides a rigorous, two-way coupling model that captures the interrelationship between geomechanical and flow properties and processes, accurately describes the system behavior, and can be readily applied to large-scale problems of hydrate behavior in geologic media.

Introduction

Background. The interrelationship between fluid flow through porous media and the geomechanical status of the system is controlled by the properties of the specifics of flow, various phases present in the pores (e.g., gas, aqueous, oil/organic, ice, etc.) and of the solid system (i.e., the individual grains of the geologic medium and the reservoir skeleton). Under certain conditions, the interrelationship is strong, and coupling of the flow processes with geomechanics is necessary to accurately describe the system behavior. In such cases, changes in pressure brought about by flow (e.g., in the process of fluid production from reservoirs) alter the stress fields, resulting in changes in porosity and permeability, and potentially leading to yielding, failures and fracture evolution or closures; these processes can in turn affect the flow behavior of the entire system. Reservoir engineering is replete with examples of such strongly coupled flow-geomechanics processes with a significant impact on production and economic consequences: stability of borehole and surface facilities, hydraulic fracturing for fluid production from low-permeability reservoirs, reservoir compaction (especially in highly compressible systems) and land surface subsidence, sand production during reservoir fluid production from unconsolidated or unstable formation, system responses during geologic CO_2 sequestration, gas production from hydrate accumulations, etc. - see Bagheri and Settari (2008), Merle et al. (1976), Lewis and Schrefler (1998), Kosloff et al. (1980), Freeman et al. (2009), Rutqvist et al. (2010b), and Rutqvist and Moridis (2009).

Hydrate reservoirs are considered as potentially substantial future energy resources (Moridis, 2003; Moridis et al., 2009a, 2011) because of the vast quantities of hydrocarbon gas (mainly CH_4) they trap (Sloan and Koh, 2008). Hydrate deposits that are desirable gas production targets almost invariably involve coarse, unlithified, unconsolidated media (such as sands and gravels). In such deposits, it is the hydrate that imparts mechanical strength to the medium, and hydrate dissociation for gas production drastically changes the geomechanical status of the system. Additionally, the system undergoes significant temperature changes because dissociation is a strongly endothermic reaction. Thus, fluid flow, heat transport and geomechanics are inexorably intertwined and need to be considered together as strongly coupled processes in hydrate accumulations under production because the inevitable significant changes in pressure P, temperature T and saturations S_J of the various phases J (aqueous, gas, hydrate, ice) during dissociation directly affect the stiffness of the solid skeleton and the stress and strain fields, resulting in deformation of the reservoirs and potentially large changes in the porosity and permeability (Rutqvist and Moridis, 2009; Rutqvist et al., 2009). Thus, in the study of gas production from hydrate deposits, the geomechanical stability and integrity of both the hydrate-bearing sediments (HBS) and the wellbore need to be considered.

Gas hydrates are solid crystalline compounds in which gas molecules are trapped within the lattice of ice crystals (Moridis, 2003). Trapped gases and the ice crystals are called *guests* and *hosts*, respectively. Given the availability of appropriate gas sources, hydrates evolve according to the exothermic equation

$$G + N_H\ H_2O = G \cdot N_H\ H_2O + Q_H, \tag{1}$$

where $G \cdot N_H H_2O$ is the hydrate, G denotes a hydrate-forming gas, N_H is the corresponding hydration number, and Q_H is the specific enthalpy of hydrate formation/dissociation. Although natural hydrates can include several guests such as CH_4, CO_2, H_2S, and N_2, CH_4 is by far the most dominant gas in natural hydrate accumulations. Hydrates are generally encountered in two distinctly different geologic settings where the conditions of low temperature T and high pressure P that favor their formation and stability are satisfied: in the Arctic and in the oceans.

The three main hydrate dissociation methods (Makogon, 1987, 1997) that can be used for hydrocarbon recovery (Moridis et al., 2009a) are as follows.

- Depressurization, which occurs when P is lowered below the pressure of hydrate stability P_e at a given T
- Thermal stimulation, which involves raising T above the dissociation temperature T_e for a given P
- Inhibitor effects, involving the use of substances such as brines and alcohols that destabilize the hydrates.

During dissociation, in addition to changes in the stress distribution, significant changes in the phase volumes occur in the pores of the HBS because of the considerable density difference between hydrates and the liquid water and gas released in the process. Thus, hydrate dissociation (or formation) can cause displacement (dilation or compaction) of the hydrate-bearing geological formation that can be pronounced in the vicinity of the well. The change in the mechanical status and properties propagates instantaneously away from the well toward the boundaries because of the nature of the quasi-static mechanics involved. In turn, the change in geomechanical status within the reservoirs can affect the reservoir fluid flow through the changes it imparts on the hydraulic properties and the corresponding.

Even though fluid flow and geomechanics need to be considered as coupled processes in order to accurately predict the reservoir behavior during gas production from hydrates, such coupling has received limited (if any) attention. Recently, Rutqvist and Moridis (2009) investigated the geomechanical effects on well stability resulting from hydrate dissociation in oceanic HBS systems caused by hot fluids from conventional deeper reservoirs intersecting extensive hydrate beds as they ascend to the surface. Their study showed that the stability of the HBS around the warm pipes and wells may be significantly affected by thermal loading. Similarly, Rutqvist et al. (2009) showed that gas production from permafrost-associated hydrates exhibited very limited displacement at the surface (and practically no danger to surface facilities and equipment) because of the protective effect of the stiff permafrost, but geomechanical changes in the HBS and in the vicinity of the well were more pronounced and could result in yielding and failure - not necessarily an adverse effect, since it had the potential of increasing the effective permeability of the HBS through development of fractures. Another study by Rutqvist et al. (2010a) investigated the stability of sloping oceanic HBS under a variety of loads (thermal and mechanical).

All these studies involved exclusively one-way (hereafter referred to as **1W**) coupling of fluid flow, heat transport and geomechanics, with the change in fluid pressure and temperature affecting mechanics, but without considering feedback from mechanics to flow through changes in the hydraulic properties. For the reasons mentioned earlier, such 1W coupling representation is not fully representative of (and often not fully appropriate for) the tightly coupled flow and geomechanics (i.e., high coupling strength; Kim et al. (2011b)) encountered in HBS, in which water is typically less compressible than the porous media, potentially affecting the quality of predictions. Two-way coupling is far more appropriate to accurately predict the behavior of such hydrate reservoirs undergoing changes.

Focus and approach. In this paper, we study two-way (hereafter referred to as **2W**) coupling between fluid flow and geomechanics in hydrate reservoirs under production as an extension of Rutqvist and Moridis (2009) and Rutqvist et al. (2009), while still employing 1W coupling between heat flow and mechanics. This is a valid approximation, justified by the large heat capacity and/or small heat contribution originating directly from the deformation of the HBS (Lewis and Schrefler, 1998).

Two representative approaches can be used to simulate the 2W coupling of fluid flow and geomechanics: the fully coupled (monolithic) method or the sequential method (Zienkiewicz et al., 1988; Armero and Simo, 1992; Settari and Mourits, 1998; Wan, 2002; Dean et al., 2006; Jha and Juanes, 2007; Jean et al., 2007). The fully coupled method can provide a stable and convergent solution, but it requires a unified flow-mechanics simulator, and a unified grid that can provide sufficient definition of both the flow and geomechanical processes. This entails an enormous software development effort, results inevitably in very large matrices, and necessitates very large memory requirements and correspondingly large computational costs.

On the other hand, the sequential implicit approach offers wide flexibility from a software engineering perspective, and uses separate software modules (and often separate grids) to handle the flow and geomechanical processes. The two robust modules communicate through a well-defined interface (Felippa and Park, 1980). However, sequential approaches may be limited by numerical stability and convergence (Armero and Simo, 1992; Armero, 1999). Here we discuss a sequential method that can provide stable solutions while being competitive in terms of accuracy with the corresponding fully coupled method.

According to Kim et al. (2011b), typical sequential techniques involve the *drained* and *fixed-strain split* methods. In the *drained split* method, the geomechanical problem (with P, T and S_J and the fluid properties and conditions kept constant, but with the fluid mass allowed to move) is solved first to estimate the displacement, followed by the solution of the coupled fluid flow and heat transport problem to determine P, T and S_J. The *fixed-strain split* method involves first the solution of the coupled problem of fluid flow and heat transport (while keeping the strain fields frozen, but allowing the total stress fields to vary) to estimate P, T and S_J, followed by the solution of the geomechanical equations to estimate the displacements.

These methods can provide – at best – conditional stability that is independent of the time step size, but may lead to non-convergence even when they are stable. Two other methods appear far more appealing: *undrained* and *fixed-stress splits*. They are both unconditionally stable, but the fixed-stress split produces more accurate solutions when flow and mechanics are tightly coupled (Kim et al., 2011b). In the *undrained split* method, the geomechanical problem (with no change in the fluid mass locally, but with the P, T and S_J varying) is solved first to estimate the displacement, followed by the solution of the coupled fluid flow and heat transport problem to determine P, T and S_J. The *fixed-stress split* method involves first the solution of the coupled problem of fluid flow and heat transport (while keeping the total stress fields frozen, but allowing the strain fields to vary) to estimate P, T, S_J, followed by the solution of the geomechanical equations to estimate the displacements.

In an isothermal problem, the fixed-stress split can be easily implemented through a simple porosity correction. The isothermal assumption is not appropriate in the description of hydrate dissociation because of the strongly endothermic nature of the reaction. Thus, we employ the fixed-stress split method with an extended porosity correction to model thermo-hydro-mechanics in hydrate deposits. This 2W coupled sequential implicit scheme of fluid flow, heat transport and geomechanics has almost the same computational cost as the 1W coupled scheme. The porosity correction is applied to the 2W coupled problem of fluid flow and geomechanics, while the coupling of heat transport and mechanics is based on a 1W scheme for the aforementioned reasons.

Expanding on the study of Rutqvist and Moridis (2009), we investigate test cases for depressurization, thermal stimulation, and plasticity. In these cases, we compare the results of the numerical simulations involving the present coupling method (i.e., 2W coupling between fluid flow and geomechanics, with 1W coupling of heat transport and geomechanics) to those obtained using the 1W coupling method used in the earlier studies. From these test cases, we determine that 2W coupling is necessary for the rigorous and accurate prediction of the overall behavior of hydrate reservoirs, in particular when investigating reservoir and well stability. The significant differences between the predictions from the 1W and the 2W coupling methods are obvious in cases of high coupling strength (i.e., involving nearly-incompressible fluids such as water), of different time scales for fluid flow and geomechanics, and low pressure-diffusion (i.e., at early times or for low permeability HBS), all of which describe most hydrate reservoirs.

Mathematical formulation

Mass and heat balance equations. In describing coupled flow and geomechanics, we employ a continuum theory, in which the fluid and solid are considered as overlapping continua. The governing equations of fluid and heat balance are based on the earlier studies of Moridis (2003) and Moridis et al. (2008) (Refer to those references for more details.), which can be written in an integrodifferential form as

$$\frac{d}{dt}\int_\Omega m^\kappa d\Omega + \int_\Gamma \mathbf{f}^\kappa \cdot \mathbf{n}\, d\Gamma = \int_\Omega q^\kappa d\Omega, \tag{2}$$

where the superscript κ denotes either a mass component or heat; m^κ, $\mathbf{f}^\kappa$, and q^κ are accumulation, flow, and source of mass of the component κ or heat in the domain Ω with a boundary surface Γ, respectively. We denote by $d(\cdot)/dt$ the time derivative of a physical quantity $(\cdot)$ relative to the motion of the solid skeleton. In long-term gas production from hydrates, Kowalsky and Moridis (2007) showed that dissociation can be accurately described as an equilibrium (as opposed to kinetic) reaction. Under these conditions, only two components need be considered: H_2O ($\kappa = w$) and CH_4 ($\kappa = m$), i.e., hydrate is considered as just one possible state of the CH_4-H_2O system. These two components are distributed among four possible phases J, i.e., aqueous ($J = A$), gaseous ($J = G$), hydrate ($J = H$), and ice ($J = I$). Then, the accumulation term m^κ ($\kappa \equiv w, m$) is given by

$$m^\kappa = \sum_{J=A,G,H,I} \phi\, S_J\, \rho_J\, X_J^\kappa, \quad \kappa \equiv w, m \tag{3}$$

where ϕ is the true porosity, defined as the ratio of the pore volume to the bulk volume in the deformed configuration; S_J and ρ_J are saturation and density of the phase J, respectively; and X_J^κ is the mass fraction of component κ in the phase J. Obviously, $X_I^w = 1$. From the hydrate stoichiometry, $X_H^w = N_H W^w/(W^m + N_H W^w)$ and $X_H^m = 1 - X_H^w$, where W^m and W^w are the molecular weights of CH_4 and H_2O, respectively.

The mass flow term $\mathbf{f}^\kappa$ in Equation 2 is given by

$$\mathbf{f}^\kappa = \sum_{J=A,G} \left(\mathbf{w}_J^\kappa + \mathbf{J}_J^\kappa\right), \tag{4}$$

where $\mathbf{w}_J^\kappa$ and $\mathbf{J}_J^\kappa$ are the convective and diffusive mass flows of component κ in the phase J. The summation over the phases J is limited to the mobile A and G, the solid phases H and I being immobile. For the aqueous phase, $\mathbf{w}_A^\kappa$ is described by Darcy's law as

$$\mathbf{w}_A^\kappa = X_A^\kappa\, \mathbf{w}_A, \quad \mathbf{w}_A = -\frac{\rho_A\, k_{rA}}{\mu_A}\, \mathbf{k}\, (\mathbf{Grad} P_A - \rho_A\, \boldsymbol{g}), \tag{5}$$

where $\mathbf{k}$ is the absolute permeability tensor; μ_J, k_{rJ}, and P_J are the viscosity, relative permeability, and pressure of the fluid phase J, respectively. $\boldsymbol{g}$ is the gravity vector, and $\mathbf{Grad}$ is the gradient operator. For the gaseous phase, $\mathbf{w}_G^\kappa$ can be written as

$$\mathbf{X}_G^\kappa = X_G^\kappa \, \mathbf{w}_G, \quad \mathbf{w}_G = -\left(1 + \frac{k_K}{P_G}\right) \mathbf{k} \, \frac{\rho_G \, k_{rG}}{\mu_G} \, (\mathbf{Grad} P_G - \rho_G \, \boldsymbol{g}), \tag{6}$$

where k_K is the Klinkenberg factor. The diffusive flow $\mathbf{J}_J^\kappa$ ($\kappa \equiv m, w; J \equiv A, G$) is described as

$$\mathbf{J}_J^J = -\phi \, S^J \, \tau_G \, \mathbf{D}_J^\kappa \, \rho_J \, \mathbf{Grad} X_J^\kappa, \tag{7}$$

where $\mathbf{D}_J^\kappa$ is the hydrodynamic dispersion tensor, and τ_G is the gas tortuosity, often computed from the Millington and Quirk (1961) model as $\tau_G = \phi^{1/3} S_G^{7/3}$.

For the heat balance equation, $\kappa \equiv \theta$, and the heat accumulation term m^θ becomes

$$m^\theta = (1 - \phi) \int_{T_0}^{T} \rho_R \, C_R \, dT \; + \sum_{J=A,G,H,I} \phi \, S_J \, \rho_J e_J, \tag{8}$$

where $\rho_R = \rho_R(T)$ and $C_R = C_R(T)$ are the density and heat capacity of the porous medium, respectively; T is the temperature; T_0 is a reference temperature; and e_J is the specific internal energy of phase J. The heat flow $\mathbf{f}^\theta$ includes conduction and convection contributions, and is described as

$$\mathbf{f}^\theta = -\mathbf{K}_\theta \nabla T + \sum_{J=A,G} h_J \, \mathbf{w}_J, \tag{9}$$

where $\mathbf{K}_\theta$ is the composite thermal conductivity of the porous media and phase J system, and h_J is the specific enthalpy of phase J. e_J and h_J are given by

$$e_J = \sum_{\kappa=w,m} X_J^\kappa \, e_J^\kappa \quad \text{and} \quad h_J = \sum_{\kappa=w,m} X_J^\kappa \, h_J^\kappa, \tag{10}$$

where e_J^κ and h_J^κ indicate the specific internal energies and enthalpies of components κ in the phase J. Note that, under equilibrium conditions, the heat of hydrate dissociation is accounted for when differencing the hydrate mass between two points in time, i.e.,

$$\Delta m^\theta = (1 - \phi) \int_{T_1}^{T_2} \rho_R \, C_R \, dT \; + \Delta(\sum_{J=A,G,I} \phi \, S_J \, \rho_J \, e_J) + H_D \, \Delta(\phi \, S_H \, \rho_H), \tag{11}$$

where T_1 and T_2 are the temperatures at these two times, and H_D is the heat of hydrate dissociation.

Geomechanics equations. Assuming a quasi-static state, the governing equation for mechanics is given by

$$\mathrm{Div} \, \boldsymbol{\sigma} + \rho_b \, \boldsymbol{g} = \mathbf{0}, \tag{12}$$

where Div is the divergence operator; $\boldsymbol{\sigma}$ is the Cauchy total-stress tensor; and $\rho_b = \phi \, \Sigma S_J \rho_J + (1 - \phi) \rho_R$ ($J \equiv G, A, H, I$) is the bulk density. Here, we assume small deformation (i.e., infinitesimal transformation) and an isotropic geomaterial.

Initial and boundary conditions. For completeness, initial and boundary conditions are needed to fully describe the problem. For fluid flow, the boundary conditions are: $P_J = \hat{P}_J$ and $X_J^\kappa = \hat{X}_J^\kappa$ (with the symbol $\hat{(\cdot)}$ indicating prescribed values, $J \equiv A, G$ and $\kappa \equiv w, m$) on the boundary of the prescribed pressure Γ_P, and $\mathbf{f}^\kappa \cdot \boldsymbol{n} = \hat{f}^\kappa$ (prescribed mass flux) on the boundary of the prescribed flow Γ_f. For well-posedness, we assume that $\Gamma_P \cap \Gamma_f = \emptyset$, and $\Gamma_P \cup \Gamma_f = \partial\Omega$. The boundary conditions for heat flow are: $T = \hat{T}$ on the prescribed temperature boundary Γ_T, and $\mathbf{f}^\theta \cdot \boldsymbol{n} = \hat{f}^\theta$ (prescribed heat flux) on the corresponding boundary Γ_θ, where $\Gamma_T \cap \Gamma_\theta = \emptyset$, and $\Gamma_T \cup \Gamma_\theta = \partial\Omega$.

In the stress equation of the geomechanical problem, the boundary conditions are as follows: $\boldsymbol{u} = \hat{\boldsymbol{u}}$ (prescribed displacement) on the prescribed displacement boundary Γ_u and $\boldsymbol{\sigma} \cdot \boldsymbol{n} = \hat{\boldsymbol{\tau}}$ (prescribed traction) on the corresponding boundary Γ_σ, where $\Gamma_u \cap \Gamma_\sigma = \emptyset$, and $\Gamma_u \cup \Gamma_\sigma = \partial\Omega$. The initial stress fields should satisfy mechanical and thermodynamic equilibriums, and be consistent with the fluid pressures, temperature, and the history of the stress-strain paths. Here, we take the initial conditions of the coupled problem as $P_J|_{t=0} = P_{J,0}$, $X_J^\kappa|_{t=0} = X_{J,0}^\kappa$ ($J \equiv A, G$, $\kappa \equiv w, m$) , $T|_{t=0} = T_0$, and $\boldsymbol{\sigma}|_{t=0} = \boldsymbol{\sigma}_0$.

Methane hydrate formation and dissociation

Applying the general Equation 1 to the case of CH_4, the dissociation/formation of methane hydrates are described as

$$CH_4 \cdot N_H H_2O \text{ (hydrate)} \leftrightarrow CH_4(\text{gas}) + N_H H_2O + Q_H \text{ (liquid or ice)}, \tag{13}$$

where N_H is the hydration number specific to the methane hydrate. The reaction of Equation 13 is depicted on the phase diagram of the water- methane- vapor(gas)-hydrate system (shown in Figure 1) as the 3-phase co-existence lines of A+G+H (when liquid water is involved) and I+G+H (when ice is involved), and includes the quadruple point Q_P.

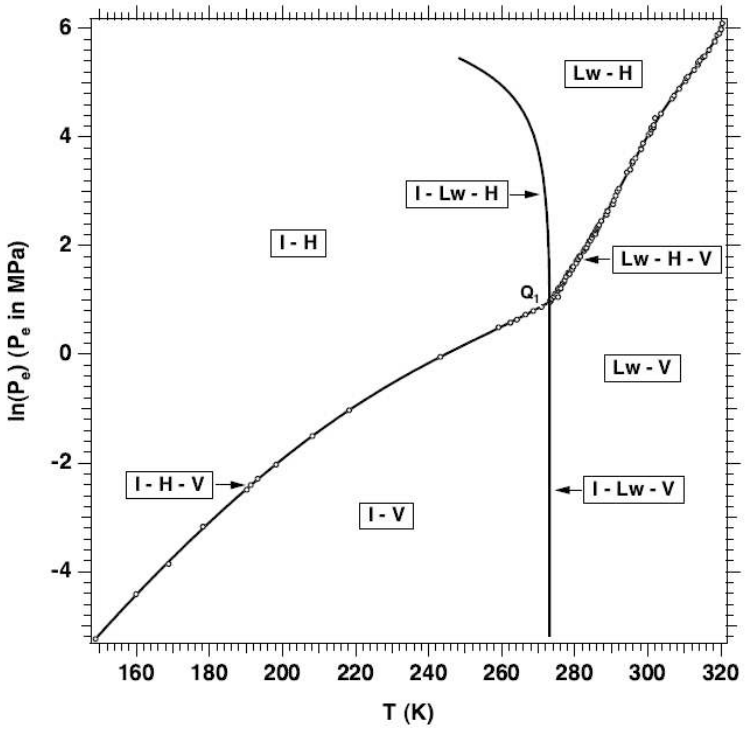

Figure 1: Pressure-temperature equilibrium relationship in the phase diagram of the water-methane-vapor-hydrate system (Moridis et al., 2008). I, V, Lw, and H indicate ice, vapor, liquid water, and hydrate phases, respectively. The dash symbol $(\cdot) - (\cdot)$ signifies coexistence of the phases. For example, $\mathrm{I} - \mathrm{H}$ means that ice and hydrate phases coexist.

From Figure 1, it is obvious that hydrates undergo dissociation when T rises to the equilibrium temperature for a given P, or P falls below the equilibrium pressure for a given T. This affects the medium dilation not only because of direct thermal expansion but also because of the decrease of the effective stress due to the increased fluid pressure. The dilation can also influence the porosity and permeability fields, the stability and integrity of the wellbore assembly, and/or the integrity of the cap rock, while at the same time affecting the flow of fluids and heat. These coupled processes between flow and geomechanics can be modeled through the constitutive relations described in the ensuing discussion.

Constitutive relations between flow and geomechanics

The constitutive relations for thermoporomechanics are based on Biot (1941) and Coussy (1995, 2004), where fluid, heat, and geomechanics are tightly coupled. The total stress $\boldsymbol{\sigma}$, fluid mass m_J, and entropy $\bar{S}$ in the elastic coupled system are functions of the total strain $\boldsymbol{\varepsilon}$, fluid pressure P_J, and temperature T, written as

$$\delta\boldsymbol{\sigma} = \underbrace{\mathbf{C}_{dr} : \delta\boldsymbol{\varepsilon}}_{\delta\boldsymbol{\sigma}'} - b_J\, \delta p_J\, \mathbf{1} - 3\alpha_T\, K_{dr}\, \delta T\, \mathbf{1}, \tag{14}$$

$$\left(\frac{\delta m}{\rho}\right)_J = b_J\, \delta\varepsilon_v + N_{JK}\, \delta p_K - 3\alpha_{m,J}\, \delta T, \tag{15}$$

$$\delta\bar{S} = \bar{s}_J\, \delta m_J + 3\alpha_T\, K_{dr}\, \delta\boldsymbol{\varepsilon}_v - 3\alpha_{m,J}\, \delta p_J + \frac{C_d}{T}\, \delta T, \tag{16}$$

where $\mathbf{C}_{dr}$ is the drained-isothermal elastic moduli; $\mathbf{N} = \{N_{JK}\}$ is the inverse matrix of the Biot moduli $\mathbf{M} = \{M_{JK}\}$ (i.e., $\mathbf{N} = \mathbf{M}^{-1}$), where $\mathbf{N}$ and $\mathbf{M}$ are positively definite matrices; $3\alpha_T$ is the volumetric skeleton thermal dilation coefficient; K_{dr}

is the drained isothermal bulk modulus; $\mathbf{1}$ is the rank-2 identity tensor; ε_v is the total volumetric strain; $\alpha_{m,J} = 3\alpha_\phi + 3\alpha_J\ \phi$, where $3\alpha_\phi$ and $3\alpha_J$ are the coefficients of thermal dilation related to porosity and the phase J, respectively; $\boldsymbol{\varepsilon}$ is the linearized total strain tensor; b_J is the Biot coefficient for phase J, determined from $b_J = bS_J$, where b is the Biot coefficient for single phase flow; $\bar{S}$ is the total entropy, and $\bar{s}_J$ is the internal entropy per unit mass of the phase J (i.e., specific entropy); $C_d = C + m_J C_{pJ}$ is the total volumetric heat capacity, where C is the skeleton volumetric heat capacity and C_{pJ} is the volumetric specific heat capacity of the phase J at constant pressure. We define $\boldsymbol{\sigma'}$, the effective stress, in the incremental form as $\delta\boldsymbol{\sigma'} = \mathbf{C}_d : \delta\boldsymbol{\varepsilon}$, where $\boldsymbol{\sigma'} = \mathbf{0}$ at $\boldsymbol{\varepsilon} = \mathbf{0}$. The symbol δ denotes variation relative to the motion of the solid skeleton. The double indices in C_d and Equations 14 – 16 indicate summation.

For a two-phase, two-component fluid system (such as oil and water), an appropriate $\mathbf{N}$ that is typically used in engineering applications is given by (e.g., Lewis and Schrefler (1998))

$$\mathbf{N} = \begin{bmatrix} \phi S_o c_o - \phi\dfrac{dS_w}{dP_c} + S_o\dfrac{b-\phi}{K_s}S_o & \phi\dfrac{dS_w}{dP_c} + S_o\dfrac{b-\phi}{K_s}\ S_w \\ \phi\dfrac{dS_w}{dP_c} + S_w\dfrac{b-\phi}{K_s}S_o & \phi S_w c_w - \phi\dfrac{dS_w}{dP_c} + S_w\dfrac{b-\phi}{K_s}S_w \end{bmatrix}, \tag{17}$$

where the subscript o and w indicate oil and water phases, respectively, c_J is the compressibility of the fluid phase J, P_c is the capillary pressure between oil and water, and K_s is the intrinsic solid grain bulk modulus.

In Equation 16, we can ignore the volumetric strain term $3\alpha_T K_{dr}\delta\boldsymbol{\varepsilon}_v$ when the heat capacity is relatively large, in which case the contribution of the direct heat source from the geomechanical deformation to the accumulation term of the heat transport equation is very small. This can justify 1W coupling between heat transport and geomechanics, allowing us to use the governing equation of heat transport with no volume change (i.e., using the fixed bulk volume Ω). However, because heat transport and fluid flow are strongly coupled, the effect of geomechanics on heat transport is still considered through the impact of geomechanical changes on fluid flow. Note that volume changes are fully considered in fluid flow (Equation 2) and geomechanics (Equation 12).

We now compare Equation 15 to the equivalent term typically used in conventional reservoir simulations (i.e., without geomechanical coupling), in which the accumulation term is described as

$$\delta m_J = \rho_J\ \Phi S_J\left(c_J\ \delta P_J - c_T\ \delta T\right) + \rho_J\ S_J\delta\Phi + \rho_J\ \Phi\delta S_J, \quad \text{where } c_J = \frac{1}{\rho_J}\frac{d\rho_J}{dP_J},\ c_T = -\frac{1}{\rho_J}\frac{d\rho_J}{dT}. \tag{18}$$

Φ is Lagrange's porosity, defined as the ratio of the pore volume in the deformed configuration to the bulk volume in the reference (initial) configuration. We can take Lagrange's porosity in Equation 17, instead of true porosity, because it is also admissible (i.e., symmetric and positively definite) and the difference is negligible. Comparing Equations 15 and 18, we have

$$\delta\Phi = \frac{b-\phi}{K_s}\sum_{J=F} S_J\ \delta P_J + b\ \delta\boldsymbol{\varepsilon}_v, \tag{19}$$

where the $J = F$ in the summation term indicates inclusion of all fluid (mobile) phases in the system. Equations 14 and 19 clearly demonstrate the tight coupling between fluid flow and geomechanics because it is obvious that volume changes cannot be ignored when estimating fluid flow. For a highly incompressible fluid (such as an aqueous phase), the coupling strength increases (Kim et al., 2011a,b), and 2W coupling is necessary to accurately describe the system behavior.

Thus, when permeability is coupled to the geomechanical status of the system, it can be estimated using a porosity-dependent permeability relationship such as that proposed by Moridis et al. (2008),

$$\mathbf{k} = \mathbf{k}_0\exp\left[\gamma_1\left(\frac{\Phi}{\Phi_0} - 1\right)\right]\left(\frac{\Phi_a - \Phi_c}{\Phi_0 - \Phi_c}\right)^{\gamma_2}, \quad \text{where} \quad \Phi_a = \Phi(S_A + S_G), \tag{20}$$

γ_1 and γ_2 are experimentally determined parameters; Φ_c is a *critical porosity* at which permeability is reduced to zero; and the subscript 0 indicates a reference state (e.g., the initial state). Note that Equation 20 involves exclusively Lagrange porosities Φ, not the true porosities ϕ. For unconsolidated, unlithified media such as those occurring in HBS that are desirable production targets, γ_1 is in the 5-7 range (Moridis et al., 2008).

From Equation 19, we can deduce that the porosity changes are not caused only by changes in the non-wetting fluid pressure, but also by saturation changes. For example, in an oil-water system, we can rewrite Equation 19 as

$$\delta\Phi = \frac{b-\phi}{K_s}\underbrace{\left(\delta P_o - S_w\frac{dP_c}{dS_w}\ \delta S_w\right)}_{\delta P_E} + b\ \delta\boldsymbol{\varepsilon}_v, \tag{21}$$

where P_c is the capillary pressure between oil and water, and P_E is the equivalent pore-pressure (Coussy, 2004). Under strong capillarity, variations in the saturation can cause changes in the Lagrange porosity even when the oil pressure does not change. Drying shrinkage of a porous medium in an air-water system is an example of such a phenomenon (Coussy et al., 1998).

Numerical schemes and simulators

For the solution of the problem of coupled fluid flow and heat transport during dissociation in the process of gas production from HBS, we employ the TOUGH+HYDRATE simulator (Moridis et al., 2008), which involves finite volume and backward Euler methods for space and time discretizations, respectively. The space discretization implemented in the code provides local mass conservation at the element level and stable pressure fields due to piecewise constant interpolation (Phillips and Wheeler, 2007a,b; Jha and Juanes, 2007). This approach has distinct advantages compared to the piecewise continuous interpolation used in finite element schemes, which may result in early-time spurious pressure oscillations in consolidation problems (Vermeer and Verruijt, 1981; Murad and Loula, 1992, 1994; Wan, 2002; White and Borja, 2008).

For the solution of the geomechanical problem, we use the "Fast Lagrangian Analysis of Continua in 3D" (FLAC3D) simulator (Itasca, 2006), which is widely used in the soil-and rock mechanics community in a wide variety of academic and engineering applications. This simulator adopts the finite difference approach, which provides first-order approximation in space and time.

Sequential approach and implementation

The two simulators described above are implemented in a sequential manner. One of the benefits of sequential implicit schemes is that the user can employ separate software modules for (a) the coupled fluid flow and heat transport and (b) the geomechanics. In sequential schemes, these two subproblems are solved in a sequence by fixing one or more state variables. For example, the total strain or total stress can be kept constant when solving the fluid and heat flow problem first. Alternatively, when the mechanical problem is solved first, one or more of fluid pressures, temperature, fluid mass, or heat can be kept constant. After the sequential solution of the subproblems, either a more accurate solution can be obtained by additional iterations, or the time can be advanced and the solution at the new time step can begin.

Kim et al. (2011c) and Kim et al. (2011d) investigated the numerical stability and convergence of the four sequential methods discussed earlier under isothermal conditions. They showed that the undrained and fixed-stress splits are unconditionally stable, and that the fixed-stress split yields higher accuracy than the undrained split, particularly under high coupling strength conditions. Based on these findings, we employ the fixed-stress split in this paper. The solution strategy of the fixed-stress split is given as

$$\begin{bmatrix} \boldsymbol{u}^n \\ \boldsymbol{p}_J^n \\ T^n \end{bmatrix} \xrightarrow{\mathcal{A}_{ss}^{fl}} \begin{bmatrix} \boldsymbol{u}^* \\ \boldsymbol{p}_J^{n+1} \\ T^{n+1} \end{bmatrix} \xrightarrow{\mathcal{A}_{ss}^{u}} \begin{bmatrix} \boldsymbol{u}^{n+1} \\ \boldsymbol{p}_J^{n+1} \\ T^{n+1} \end{bmatrix}, \quad \text{where} \quad \begin{cases} \mathcal{A}_{ss}^{fl} : \text{Fluid and heat flow; } \delta\dot{\sigma} = 0, \\ \\ \mathcal{A}_{ss}^{u} : \text{ Mechanics; } P_J,\ T : \text{prescribed}, \end{cases} \tag{22}$$

where $\mathcal{A}_{ss}^{F}$ and $\mathcal{A}_{ss}^{U}$ stand for the fluid-and-heat flow and the mechanics steps, respectively. $\boldsymbol{u}^*$ is an intermediate displacement, but there is no need to calculate or store it.

During the A_{ss}^{fl} step, combining the constraint $\delta\dot{\sigma} = 0$ with Equation 19 under the backward Euler method yields

$$\begin{aligned} \Phi^{n+1} - \Phi^n &= \underbrace{\left\{ \frac{b^2}{K_{dr}} + \frac{b-\phi}{K_s} \right\}}_{\Phi c_p} \sum_{J=F} S_{J,e}^{n+1} \left(p_J^{n+1} - p_J^n \right) + 3\alpha_T b \left(T^{n+1} - T^n \right) - \Delta\Phi, \quad S_{J,e} = \frac{S_J}{\sum_{J=F} S_J}, \\ \Delta\Phi &= \frac{b^2}{K_{dr}} \sum_{J=F} S_{J,e}^{n} \left(p_J^{n} - p_J^{n-1} \right) + 3\alpha_T b \left(T^{n} - T^{n-1} \right) - b \left(\varepsilon_v^n - \varepsilon_v^{n-1} \right) \\ &= -\frac{b}{K_{dr}} \left(\sigma_v^n - \sigma_v^{n-1} \right), \end{aligned} \tag{23}$$

where $\Delta\Phi$ is the porosity correction term; σ_v is the volumetric (mean) total stress; and $n-1$, n and $n+1$ denote three successive points in the discretized time domain. $\sum_{J=F} S_J$ is the sum of fluid (mobile) phase saturation, where F implies fluid (mobile) phase. The term c_p in Equation 23 represents the pore compressibility that is routinely used in conventional simulators (i.e., not considering geomechanics rigorously). The porosity correction term $\Delta\Phi$ is ignored in conventional reservoir simulators (and even when 1W coupling of fluid flow and geomechanics is implemented), but needs to be considered in a tightly coupled problem.

Note that the porosity function in the 1W coupling scheme still depends on the liquid phase saturation S_J and the drained bulk modulus K_{dr}, just as the 2W coupling scheme does. The K_{dr} in 1W coupling realizations is estimated from the mechanics boundary conditions. In the 2W coupling scheme, when K_{dr} cannot be determined exactly because of complex boundary conditions or high mechanical nonlinearity, it is estimated as less stiff than the true local bulk modulus (Kim et al., 2011d). For example, it is possible to use the constrained modulus for the porosity function in 2W coupling; the same could be used in 1W coupling, and is stiffer than the true bulk modulus. This approximate estimation of K_{dr} in 2W coupling schemes may cause numerical instability or non-convergence by violating the numerical stability criterion determined by Kim et al. (2011d). We will demonstrate this numerical behavior with three-dimensional numerical examples in a later section.

For elastoplasticity, the elastoplastic tangent bulk modulus is estimated from the relationship (Kim et al., 2011d)

$$K_{dr}^{ep} = K_{dr}^{e}\frac{\varepsilon_{v,e}}{\varepsilon_v},\ \varepsilon_{v,e} = \varepsilon_v - \varepsilon_{v,p}, \tag{24}$$

where K_{dr}^{e} and K_{dr}^{ep} are the elastic and elastoplastic drained bulk moduli, respectively, and $\varepsilon_{v,e}$ and $\varepsilon_{v,p}$ are the elastic and plastic volumetric strains, respectively.

For the oil and water system discussed earlier, Equation 23 can be written as

$$\Phi^{n+1} - \Phi^{n} = \underbrace{\left\{\frac{b^2}{K_{dr}} + \frac{b-\phi}{K_s}\right\}}_{\Phi c_p}\left\{\left(P_o^{n+1} - P_o^{n}\right) - S_w^{n+1}\frac{dP_c}{dS_w}\left(S_w^{n+1} - S_w^{n}\right)\right\} + 3\alpha_T\, b\left(T^{n+1} - T^{n}\right) - \Delta\Phi, \tag{25}$$

where P_o, S_w, and T are chosen as the primary variables for the solution of the problem.

In reservoir simulation, 2W coupling between fluid flow and geomechanics has been implemented through the porosity function and its correction term (Settari and Mourits, 1998; Tran et al., 2004). However, the pore pressure in these studies is not clearly defined. For example, the approach proposed by Settari and Mourits (1998) becomes identical to Equation 25 for linear elasticity only when the pore pressure in Settari and Mourits (1998) is defined as the equivalent pore-pressure employed in this paper. If the pore pressure is defined as the oil pressure, the approach of Settari and Mourits (1998) neglects the term related to capillary pressure in Equation 25, which is associated with deformation of porous media caused by changes in the water saturation and is akin to drying-related shrinkage in air-water systems. If the pore pressure is defined as the average pore-pressure (a widely used approach in many engineering fields, e.g., Wan (2002) and Gai (2004)), large errors or numerical instability can result when strong capillarity is involved; conversely, using the equivalent pore-pressure defined by Coussy (2004) in Equation 21 yields numerical stability and accuracy. The interested reader is refered to Kim et al. (2011a) for a detailed discussion of the concepts of the average and equivalent pore pressures.

The computational efforts for 1W and 2W couplings are almost the same. The additional computational cost associated with 2W coupling involves only the local calculation of Lagrange's porosity correction term $\Delta\Phi$, which is negligible when compared to the global computational cost. In terms of memory requirement, the 2W coupling approach necessitates the allocation of additional memory only for P_J, T, and S_J (or the volumetric (mean) total stress) at the $n-1$ time step. The porosity function is updated anyway, and the code modification is easy and straightforward.

Numerical examples

We first tested the coupled TOUGH+HYDRATE and FLAC3D codes – hereafter referred to as THF, and incorporating both 1W and 2W coupling options with correspondingly different constitutive relationships – in the validation of the classical problems of Terzaghi (Wang, 2000) and Mandel (Abousleiman et al., 1996). We then obtain the THF solutions of representative 2D and 3D problems of system behavior during gas production from HBS, involving the coupled processes of hydrate dissociation, fluid flow, strong heat exchanges and the corresponding geomechanical system responses. In the validation studies and in all subsequent test cases we employ the staggered method with one iteration, also called the sequential non-iterative method. In all subsequent numerical studies, we use $\gamma_1 = 0$, $\gamma_2 = 3.0$ and $\Phi_c = 0$ in Equation 20.

Validation. Figures 2a and 2b describe the Terzaghi problem and an approximation to the Mandel problem, respectively. Thorough descriptions and analytical solutions to the Terzaghi and Mandel problems are presented in Wang (2000) and Abousleiman et al. (1996), respectively.

The instantaneous pressure buildup at $t = 0$ in the Terzaghi problem, or the initial pressure rise in the Mandel problem cannot be handled by 1W coupling because this approach is incapable of providing (and solving) the appropriate constitutive relations that accurately describe the two problems. Two-way coupling between fluid flow and geomechanics involves the appropriate – also more scientifically and numerically robust – equations and yields accurate solutions, capturing the consolidation effects in the two aforementioned problems. Thus, 2W coupling provides more rigorous constitutive relations than 1W coupling.

The Terzaghi problem (see Figure 2a) involves a 1-D system (column) of a water-saturated porous medium, with drainage boundary at the top of the domain (where the fluid pressure is $P_{bc} = 10\ MPa$) and a no-flow boundary at the bottom. The total stress imposed by the overburden at the top boundary is $\bar{\sigma} = 2 \times 10\ MPa$, and a no-displacement boundary condition is applied at the bottom. The homogeneous domain has a length of $L_z = 18\ m$, and is subdivided into 9 grid blocks of uniform size $\Delta z = 2\ m$. In all gridblocks, $\Delta x = \Delta y = 1m$. The initial temperature and fluid pressure are $T_i = 12.5\ ^oC$ and $P_i = 10\ MPa$, respectively. The water thermophysical properties (density, viscosity, and compressibility) are determined from steam tables as functions of P and T. The permeability of the porous medium is $k_0 = 5.92 \times 10^{-14}\ m^2 (= 60\ md)$, the porosity is $\phi_0 = 0.3$, the constrained modulus is $K_{dr} = 900\ MPa$, and the Biot coefficient is $b = 1.0$. The system specifications include (a) no fluid production or injection, (b) omission of gravitational effects, and (c) an observation point at the bottom grid block. Instantaneous loading at $t = 0$ results in an increase in P, followed by a decrease (dissipation) caused by pressure diffusion, as shown in the left of Figure 3. We assign much stiffer mechanical properties to the top layer to conform to the boundary conditions used in

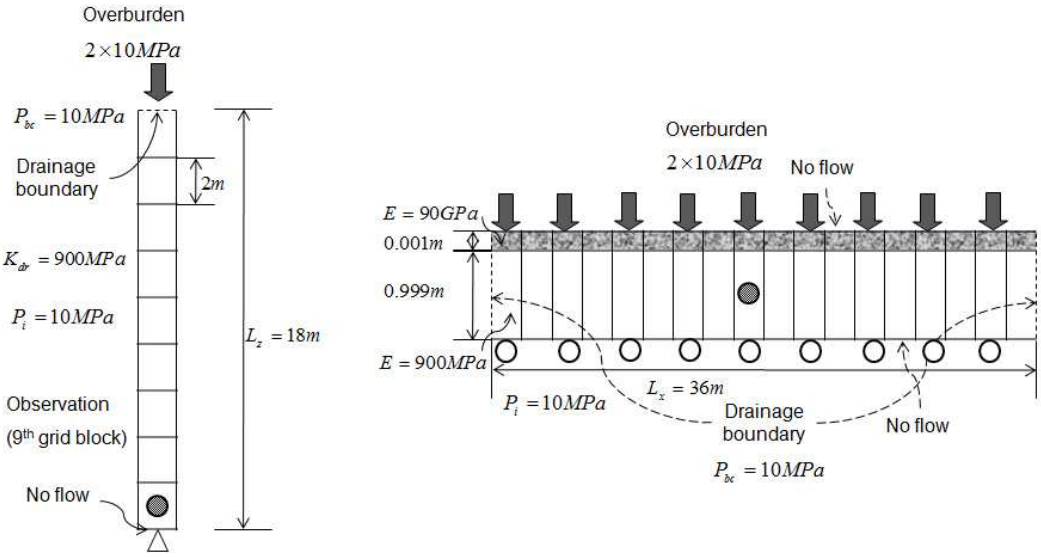

Figure 2: Configurations of the Terzaghi (a) and Mandel (b) problems. The triangles and circles at the boundaries of the two domains denote fixed displacement and rollers to constrain displacements, respectively.

the Abousleiman et al. (1996) study (see Figure 2b) that yield an analytical solution, to which the THF solution is compared. This approximation is equivalent to the penalty method, a mathematical approximation for solving mechanics with constraints (Hughes, 1987). The homogeneous domain is subdivided into 18×2 grid blocks in (x, z). The thickness and the Young's modulus of the first and second layer are $\Delta z = 0.001\ m,\ E = 90\ GPa$ and $\Delta z = 0.999\ m,\ E = 900\ MPa$, respectively. The geomechanical boundary conditions include (a) an overburden-induced total stress at the the top $\bar{\sigma} = 2 \times 10\ MPa$, (b) no horizontal displacement at the center, and (c) no vertical displacement at the bottom (see Figure 2b). Both x-boundaries have a side burden of $\bar{\sigma}_h = 10\ MPa$. The initial temperature and fluid pressure are $T_i = 12.5\ ^oC$ and $P_i = 10\ MPa$, respectively. The medium properties are as follows: $\phi_0 = 0.3$, Poisson's ratio $\nu = 0.0$, $b = 1.0$, a horizontal permeability $k_{x0} = 6.02 \times 10^{-15} m^2 (= 6.1\ md)$, and a very high permeability $k_{z0} = 5.0 \times 10^{-6}\ m^2 (= 5.07 \times 10^6\ md)$ in the vertical direction to facilitate horizontal fluid flow. The system specifications also include (a) drainage boundaries at $x = 0$ and $x = x_{max}$ kept at a constant boundary fluid pressure of $P_{bc} = 10\ MPa$, (b) no-flow boundaries at the top and bottom of the domain, (c) omission of gravitational effects, and (d) an observation point at the central gridblock (i.e., (row, column)=(2, 9)). The pressure rises at an early t because of multi-dimensional mechanics (the Mandel-Cryer effect), as shown in Figure 3.

Comparison of the THF to the analytical solutions of the two validation problems shows (a) coincidence in the Terzaghi problem (Figure 3a), and (b) an excellent match in the Mandel problem. The small differences between the numerical and analytical solution at early times in Figure 3b are due to the approximation of boundary conditions in the Mandel problem.

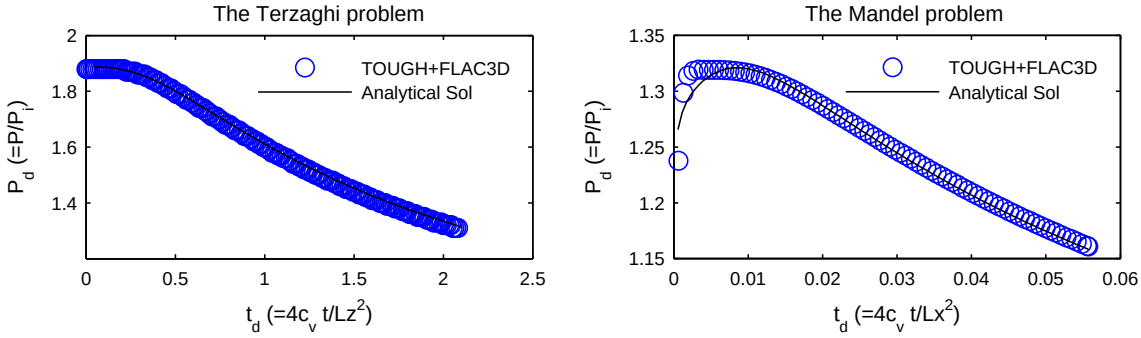

Figure 3: Comparison of the THF solutions to the analytical solutions of (a) the Terzaghi problem (Wang, 2000) on the left, and (b) the Mandel problem (Abousleiman et al., 1996) on the right. $t_d = \frac{4c_v t}{(L_z)^2}$ and $t_d = \frac{4c_v t}{(L_x)^2}$ for the Terzaghi and Mandel problems, respectively, where c_v is the consolidation coefficient defined as $c_v = \frac{k_0}{(1/K_{dr} + \phi c_A)\mu_A}$. c_A and μ_A are the compressibility and viscosity of the aqueous phase. L_z and L_x are vertical and horizontal lengths of the reservoir domains, respectively.

Two-dimensional test problem. The first test problem involves gas production by means of depressurization-induced dissociation from a hydrate accumulation using a horizontal well, and is depicted in Figure 4. Although the reservoir depicted in

Figure 4a is a 3D system, because of symmetry about the $x = 0$ axis and the assumption of uniformity along the y-direction, only the 2D subdomain (single slice, with $\Delta y = 10\ m$) of the domain shown in Figure 4b need be simulated (i.e., the plane strain mechanics (Rutqvist and Moridis, 2009)). This 2D domain is subdivided into 20×10 uniformly-sized gridblocks in (x, z), with gridblock dimensions of $\Delta x = 10\ m$, $\Delta y = 10\ m$, and $\Delta z = 10\ m$. For a solid saturation $S_s (\equiv S_H + S_I) = 0$, the Young's modulus and the Poisson's ratio are $E = 200\ MPa$ and $\nu = 0.15$, but $E = 1.4\ GPa$ and $\nu = 0.15$ for a full solid saturation, i.e., $S_s = 1$. For a given S_s $(0 < S_s < 1)$, E and ν are obtained from a linear interpolation between the two S_s limits (Rutqvist and Moridis, 2009). Other medium properties are: $\rho_b = 2600\ kg\ m^{-3}$, $\phi_0 = 0.3$, $b = 1.0$, $P_c = 0$, a medium specific heat of $C_R = 1000\ Jkg^{-1}\ ^oC^{-1}$, a *wet* thermal conductivity $k_{\theta w} = 3.1\ Wm^{-1}\ ^oC^{-1}$, a *dry* thermal conductivity of $k_{\theta d} = 0.5\ Wm^{-1o}C^{-1}$, and a composite thermal conductivity computed from the Moridis et al. (2005) relationship. The initial conditions are: $P_i = 9.71\ MPa$, $T_i = 12.5\ ^oC$, a hydrate saturation $S_H = 0.5$, and an aqueous saturation $S_A = 0.5$. The system has no-flow boundaries on all sides. The geomechanical boundaries include no-horizontal displacement boundaries at $x = 0$ and $x = x_{max}$, no-vertical displacement boundaries at the bottom, an overburden-induced principal total stress of $\bar{\sigma} = -9.71\ MPa$, and no strain at $t = 0$.

We consider two cases: A high-permeability case with $k_0 = k_{0,max} = 2.96 \times 10^{-13} m^2 (= 300\ md)$, and a low-permeability case with $k_0 = k_{0,min} = 2.96 \times 10^{-15} m^2 (= 3\ md)$. We investigate the performance of the coupled THF simulations with both 1W and 2W coupling capabilities in the analysis of a variety of problems: depressurization-induced dissociation and fluid flow, both neglecting and accounting for gravitational effects, in which case the pressure distribution with depth follows the hydraulic pressure gradient, with $P_i = 9.71\ MPa$ at the top layer; system response behavior during thermal loading; and an evaluation of the role of plasticity. We determine the sensitivity of the THF solutions to several important variables, parameters and conditions, and we compare the solutions obtained using both 1W and 2W couplings. For 1W coupling and elastic conditions, the drained modulus for the rock compressibility K_{dr} is the constrained modulus K_{dr}^C because of the horizontally constrained boundary condition, which produces more accurate results than other possible K_{dr} estimates; for 2W coupling under elastic conditions, the K_{dr} estimate is obtained from the 3D drained bulk modulus K_{dr}^{3D}. The terms K_{dr}^C and K_{dr}^{3D} are defined as

$$K_{dr}^C = \frac{E(1-\nu)}{(1+\nu)(1-2\nu)}, \qquad K_{dr}^{3D} = \frac{E}{3(1-2\nu)}. \tag{26}$$

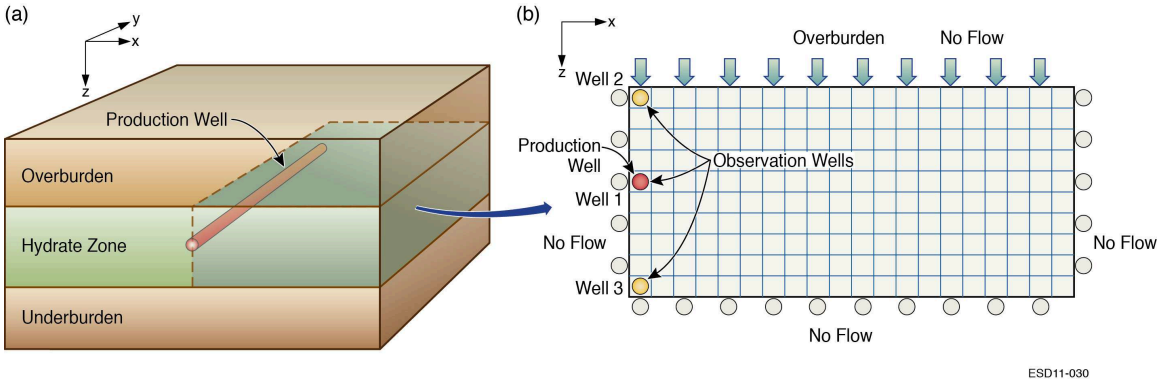

Figure 4: 2D problem of depressurization-induced gas production from a hydrate deposit using a single horizontal well: (a) overall system description (left), and (b) description of the simulated domain, and of the flow and geomechanical boundary conditions (right).

Depressurization-induced hydrate dissociation and reservoir fluid production. We first investigate the behavior of the elastic reservoir in Figure 4 in order to understand the interrelation between fluid flow, heat transfer and geomechanics in hydrate reservoirs under depressurization-induced production. Gravitational effects are ignored in this first study. The nonlinear elasticity is driven by the change in the solid saturation S_s, even though the rock itself is linearly elastic. Reservoir fluids are produced from Well 1 at the gridblock located at (row, column) = (5, 1) at a total mass rate of $Q_p = 5.0 \times 10^{-2} kg/s$ (see Figure 4b). Q_p includes both gas and aqueous phase contributions. There are two monitoring wells: Well 2 at (1, 1) and Well 3 at (10, 1).

In Figure 5 we compare the THF solutions at two observation points (Wells 1 and 3), using 1W and 2W couplings for the high reservoir intrinsic permeability, i.e., when $k_0 = k_{0,max}$. The variable t_d on the x-axis of the graphs in Figure 5 is defined as $t_d = Q_p t / M_i$ (where M_i is the initial reservoir mass-in-place), and represents the produced reservoir fluids as a fraction of M_i while at the same time providing a direct measure of the time to reach that point because Q_p is constant. At $t_d \approx 1.0 \times 10^{-3}$, gas evolves in the hydrate deposit (i.e., $S_G > 0$) at the locations of both Wells 1 and 3 (not shown in this paper). Because of continuous production, the pressure in the system declines monotonically. The evolution of pressures at Wells 1 and 2 (Figures 5a and 5b) is described by the relative (dimensionless) pressure $P_d = P_A / P_i$, i.e., as a fraction of the original (discovery) reservoir pressure P_i, and indicates practical coincidence of the THF solutions for 1W and 2W couplings over the entire domain because the fast diffusion of pressure (caused by the large $k_{0,max}$) prevails over the mechanics-induced

change in pressure. Similarly, the volumetric strains ε_v in Figures 5c and 5d from the 1W and 2W coupling formulations are shown to be practically identical at these two (as well as at all other) locations in the domain.

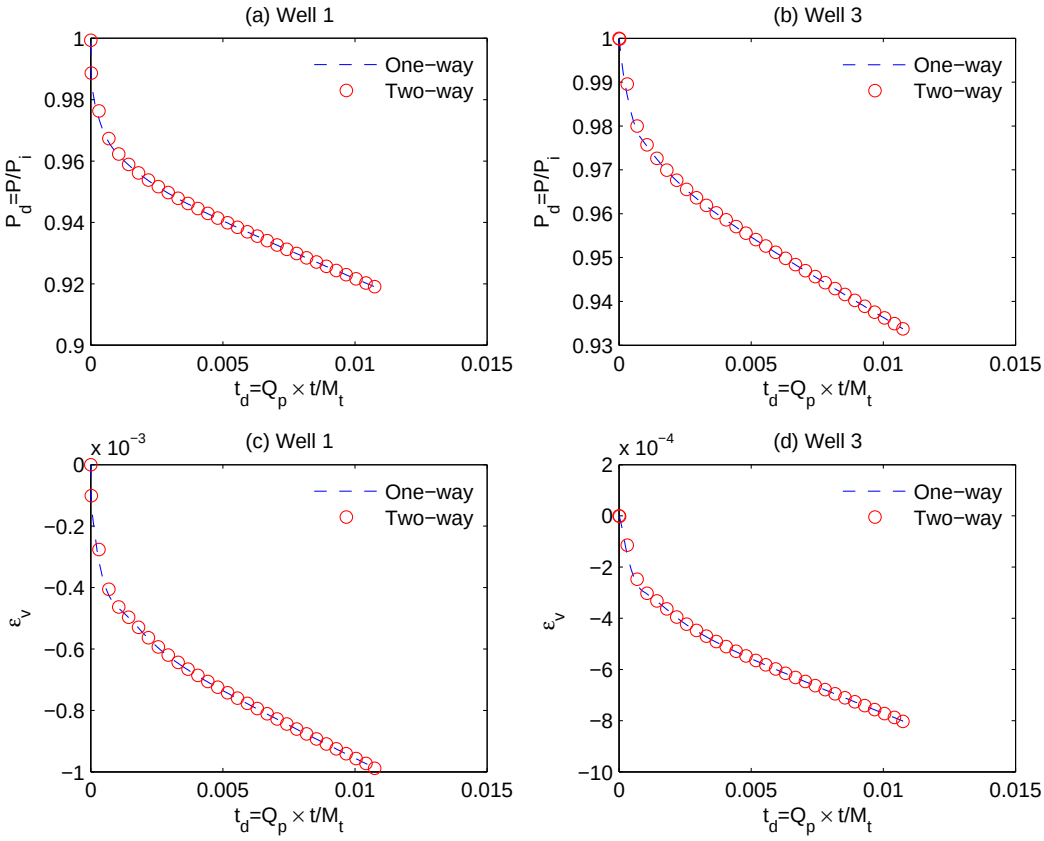

Figure 5: Comparison of the THF solutions for the high-permeability ($k_0 = k_{0,max}$) case of the 2D problem using one-way (1W) and two-way (2W) coupling formulations: (a) Pressure evolution at Well 1; (b) Pressure evolution at Well 3; (c) Evolution of the volumetric total strain ε_v at Well 1; and (d) Evolution of ε_v at Well 3.

The analogous THF solutions in Figure 6 correspond to the low permeability case ($k_0 = k_{0,min}$) and paint a very different picture, exhibiting substantial differences between the predictions based on 1W and 2W couplings. In this case, compaction or dilation of the reservoir occurs predominantly due to slow pressure diffusion and loading effects resulting from the production of fluids. There is no difference between the P_d predictions from the two coupling methods at the production Well 1 (Figure 6a). However, fluid production transfers increasingly large mechanical loads from the reservoir fluids to the reservoir skeleton, thus generating mechanical loading that results in compaction at the locations of Wells 2 and 3.

When invoking the 2W coupling formulation, the reservoir compaction and slow pressure diffusion at early times lead to the pressure buildup observed at the locations of Wells 2 and 3, shown in Figures 6 (b) and (c). The pressures at Wells 2 and 3 begin decreasing after a relatively short time because of pressure diffusion, and exhibit significant deviations from the 1W solutions at all times during the simulation period. This pressure behavior cannot be captured by 1W coupling, which is incapable of describing the effects of geomechanics on flow.

Figure 6(d) shows the different propagation pathways of the effective stresses (i.e., σ'_m and τ'_m) at Well 3, as estimated using the 1W and 2W coupling methods, where

$$\sigma'_m = \frac{\sigma'_1 + \sigma'_3}{2} \quad \text{and} \quad \tau'_m = \frac{\sigma'_1 - \sigma'_3}{2},$$

and σ'_1 and σ'_3 are the maximum and minimum principal effective stresses, respectively. If the Mohr-Coulomb failure criterion is defined by a cohesion of $c_h = 0.15\ MPa$ and a friction angle of $\Psi_f = \pi/6$ (represented by the MC line in Figure 6(d)), the shear failure that occurs at $t_d = 1.4 \times 10^{-3}$ can be detected by the 2W coupling, but is completely missed by the 1W coupling method.

In addition to changes in pressure, the strongly coupled processes involved in hydrate dissociation result in significant changes in a wide range of flow and thermodynamic parameters and conditions. Some of them are shown in Figure 7, which provides additional insights into the differences between the THF solutions at the Well 2 location using 1W and 2W coupling schemes for the $k_0 = k_{0,min}$ case of the 2D problem. As is obvious from Figure 7(b), no gas evolves in 1W and 2W predictions.

Invoking the 2W coupling scheme, the pressure increase in Well 2 (see 5(b)) leads to an increase in the temperature that exceeds the initial one T_i (as described by the relative temperature $T_d = T/T_i > 1$ for $t_d < 2.3 \times 10^{-3}$; see Figure 7(a)) because of the coupling between the equilibrium dissociation P_e and T_e (Figure 1). Similarly, the evolution of hydrate saturation S_H in Figure 7(c) to levels above its initial value shows that the 2W scheme predicts the formation of secondary hydrate at times that correspond to the higher P at Well 2 (Figure 7(c)), which is consistent with expectations, indicates that the rise in P outweighs the counter-effects of a rising T, and leads to the lower effective permeability k_p of Figure 7(d). The 1W coupling method is unable to describe the rises in T, P, and S_H, as well as the corresponding decline in k_p, that the 2W scheme captures.

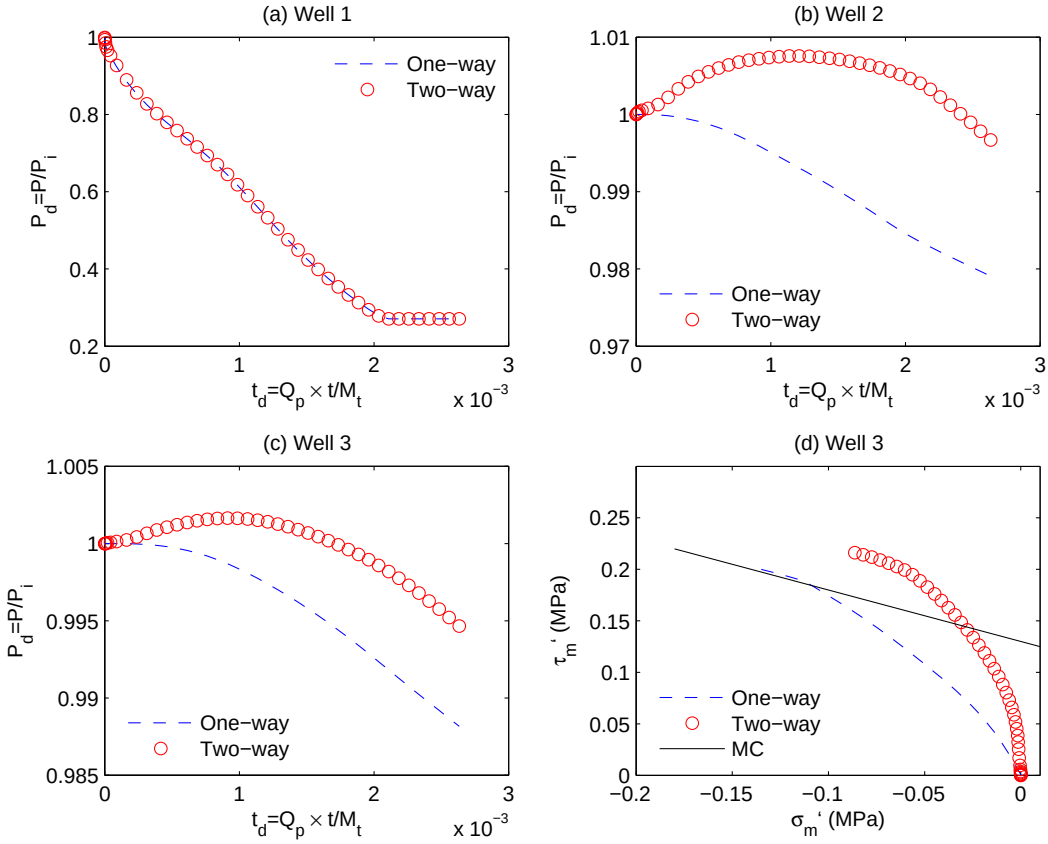

Figure 6: Comparison of the THF solutions in the low-permeability ($k_0 = k_{0,min}$) case of the 2D problem using one-way (1W) and two-way (2W) coupling formulations: (a) pressure evolution at Well 1; (b) pressure evolution at Well 2; (c) pressure evolution at Well 3; and (d) effective stress propagation at Well 3. The MC line indicates the Mohr-Coulomb model. Note that the tensile stress is positive.

To further analyze the different behaviors predicted with the two coupling methods, we repeat the $k_0 = k_{0,min}$ 2D study but now using a modified domain, i.e., one in which the gridblocks have the same Δx and Δy, but a uniform and smaller $\Delta z = 1.0\ m$, resulting in an aspect ratio for the entire domain that, at 20:1, is higher than the one discussed in the earlier 2D problem. The THF results in Figure 8 exhibit the same characteristics identified in Figure 6 in terms of the differences in behavior between the 1W- and 2W-associated predictions. Away from the production well (Figure 8 (a)), the pressure rises at early times because of compaction, and then decreases due to pressure diffusion. Figure 8(b) indicates that, if elastoplasticity is described by the Mohr-Coulomb model with $c_h = 0.05\ MPa$ and $\Psi_f = \pi/6$, 2W coupling can capture failure at earlier time ($t_d = 9.3 \times 10^{-5}$) than 1W coupling.

Fundamentally, the differences between the solutions from 1W and 2W couplings in the THF simulations are a consequence of the characteristics of quasi-static mechanics, which result in different time scales for fluid flow and geomechanics. That is, a perturbation at any given point (including boundary points), e.g., a change caused by production in flow, or by traction in mechanics, affects the entire domain as it propagates with the infinite speed of sound, and changes instantaneously the flow conditions, parameters and properties such as pressure, saturation, temperature, porosity, and permeability in the entire domain. Additionally, when changes in the mechanical moduli (e.g., bulk and shear moduli) occur due to changes in hydrate and/or ice saturation, the total and the effective stresses are redistributed, affecting in turn the distribution of strain, porosity, and permeability in the domain. As a result, 2W coupling between mechanics and fluid flow is necessary if it is important to capture the complicated reservoir behaviors described above, while 1W coupling simplifies or averages all the reservoir coupled processes. This simplification or averaging is more pronounced in low permeability fields.

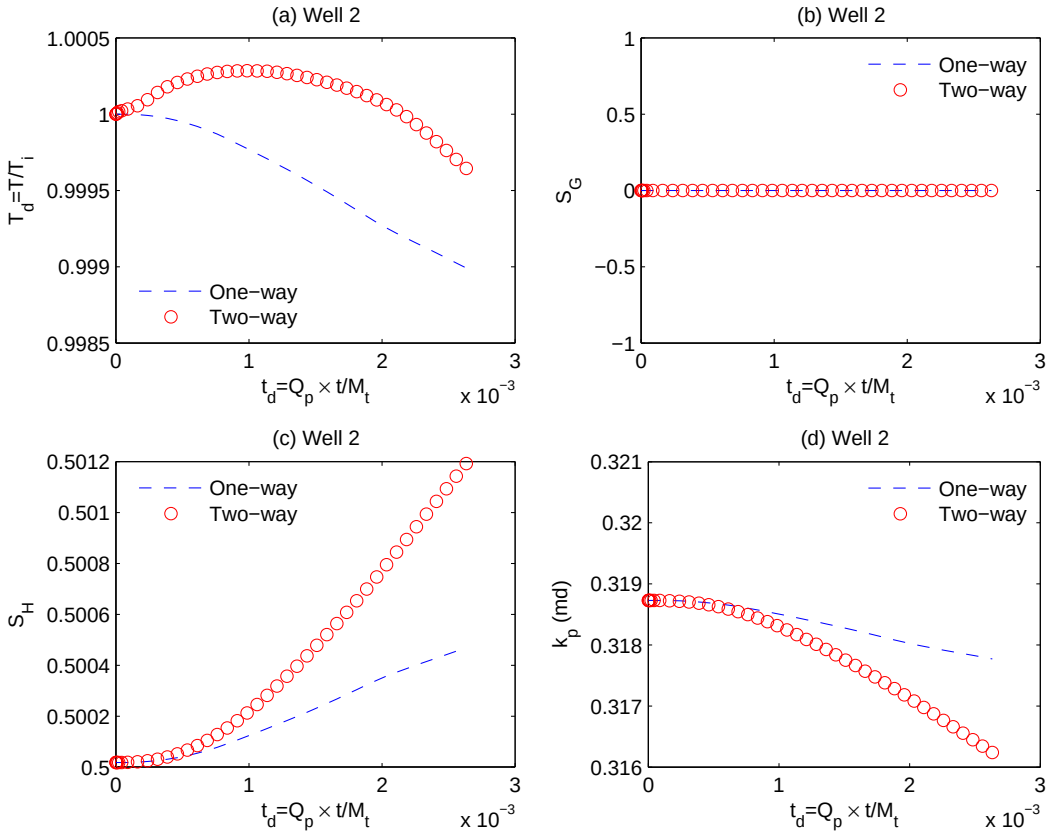

Figure 7: Comparison of the THF predictions of important variables and conditions at the location of Well 2 in the low-permeability ($k_0 = k_{0,min}$) case of the 2D problem using one-way (1W) and two-way (2W) coupling formulations: (a) relative temperature T_d; (b) gas saturation S_G; (c) hydrate saturation S_H; and (d) effective permeability k_p. The differences between the 1W and 2W predictions are attributed to reservoir compaction and slow pressure diffusion.

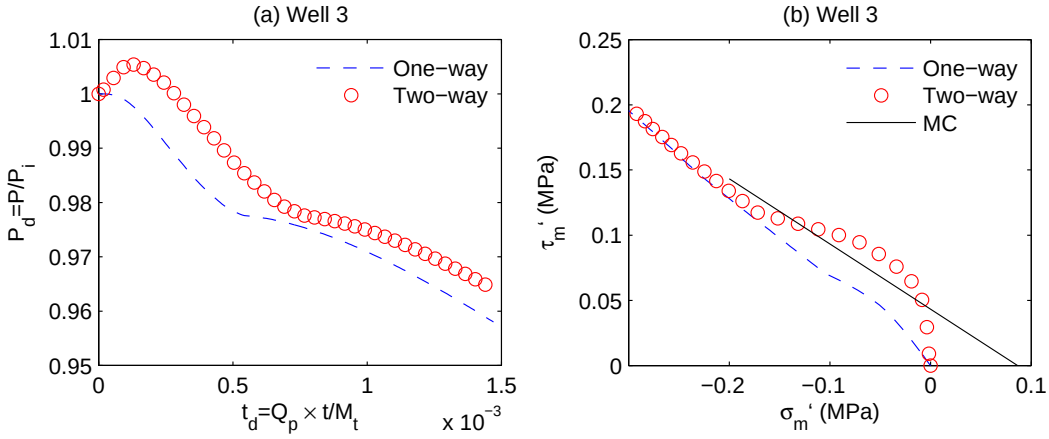

Figure 8: Evolution of (a) pressure and (b) effective stresses at Well 3 during the THF simulation of the $k_0 = k_{0,min}$ system and a high aspect ratio (20:1). We observe differences between 1W and 2W coupling methods.

Thermal loading. In depressurization-induced dissociation, it may be necessary to inject heat directly into the 2-D domain through the production well (e.g., electrical heating) during production in order to avoid the formation of ice or secondary hydrate in the vicinity of the well. Evolution of these solid phases could significantly reduce permeability, inhibit flow, and even ultimately result in complete flow blockage.

We investigate the performance of the two coupling methods in the THF simulator in the case of thermal loading resulting from direct heat injection at a rate of $Q_h = 2.0 \times 10^4\ W$ into Well 1 of the 2-D system with $k_0 = k_{0,min}$ that we described earlier (Figure 4). Figure 9 shows the evolution of P_d, T_d and ε_v at the production well (Well 1) and at the bottom observation well (Well 3). The two coupling methods yield the same results at Well 1 (Figure 9 (a)), but we observe a different behavior at Well 3 (Figures 9 (b), (c), and (d), with significant deviations between the 1W and 2W predictions). The temperature at Well 3 increases initially slightly above T_i due to the thermodynamic equilibrium constraint and the higher pressure, which builds up because of reservoir compaction and the undrained condition at early times (Figure 9 (b), (c), and (d)).

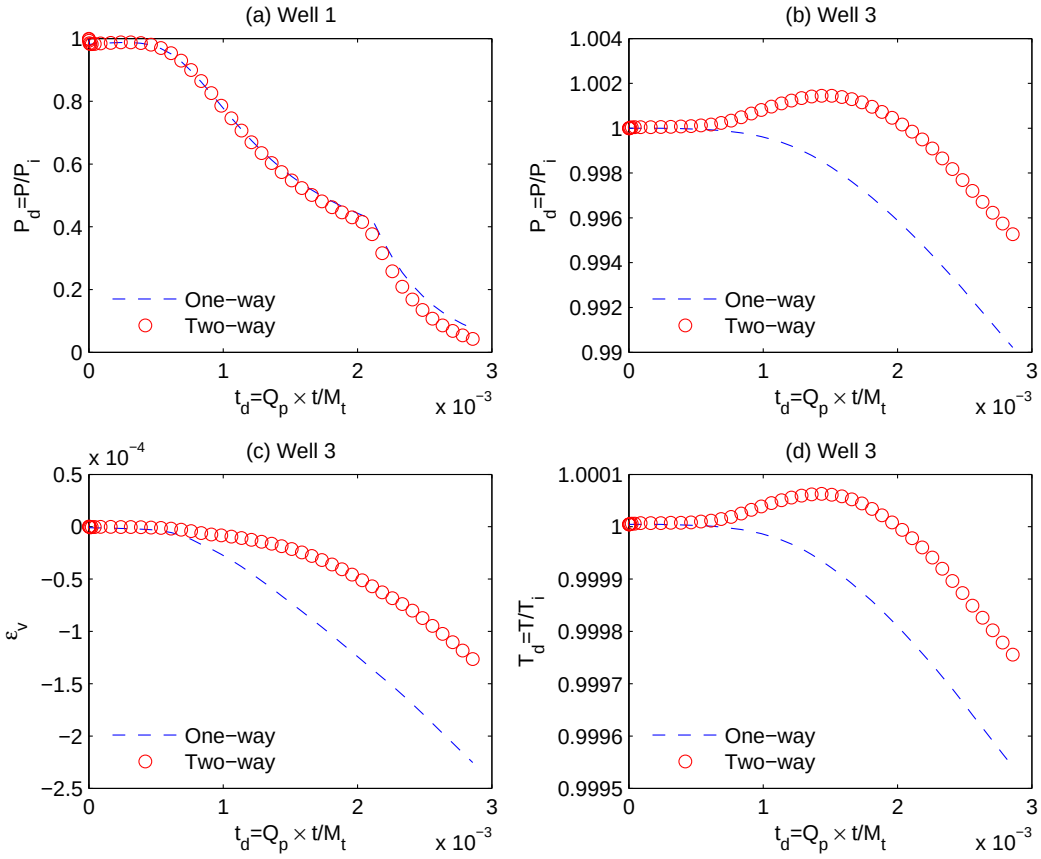

Figure 9: Comparison of the 1W and 2W formulations in the THF solutions in the low-permeability ($k_0 = k_{0,min}$) case of the 2-D problem with thermal loading: (a) pressure evolution at Well 1; (b) pressure evolution at Well 3; (c) evolution of total volumetric strain at Well 3; and (d) effective stress propagation at Well 3. Note the proximity of the two solutions at Well 1 (the production well), and the significant deviations at the location of Well 3 (see Figure 4b).

Plasticity and geological stability. Using the 2-D system shown in Figure 4, we investigate the behavior of nonlinear elastic reservoirs, in which the nonlinearity of mechanics results from the change in solid saturation (i.e., hydrate and/or ice). In this section, we study the geomechanical stability of the hydrate reservoirs, introducing elastoplasticity. We employ the Mohr-Coulomb model for elastoplasticity (embedded in the FLAC3D component of THF), which is widely used to model failure in cohesive frictional materials. The yield criterion f and the plastic potential function g are written as

$$f = \tau'_m - \sigma'_m \sin\Psi_f - c_h \cos\Psi_f \leq 0, \tag{27}$$

$$g = \tau'_m - \sigma'_m \sin\Psi_d - c_h \cos\Psi_d \leq 0,$$

where Ψ_d is the dilation angle.

As shown in Figure 10, the yield function of the Mohr-Coulomb model includes six corners and a common vertex on the

tension side of the hydrostatic axis. The discontinuous corners may cause numerical instability in return mapping (Borja et al., 2003; Wang et al., 2004).

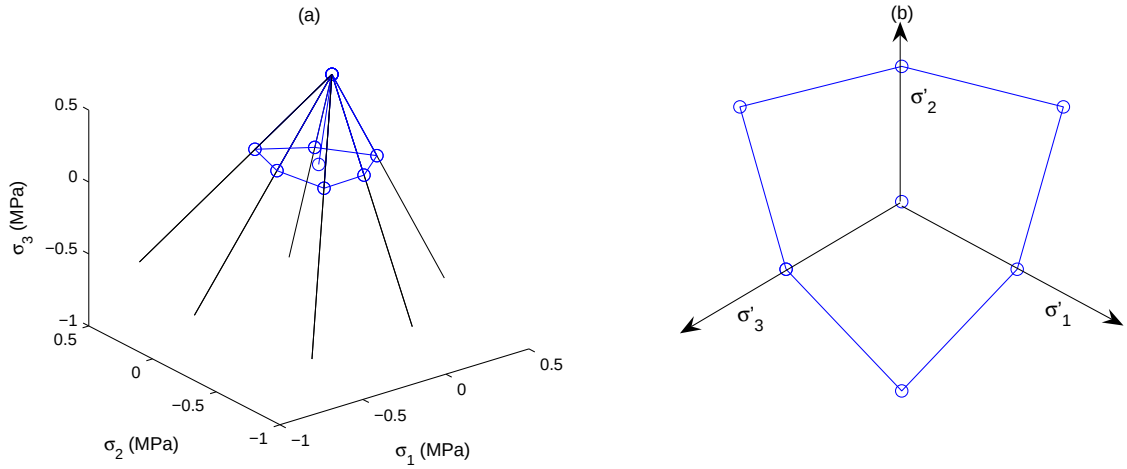

Figure 10: Mohr-Coulomb yield surface on (a) the principle effective stress space, and (b) on the deviatoric plane. σ'_1, σ'_2, and σ'_3 are the principal effective stresses. All the effective stresses are located inside the yield surface.

We use again the reservoir domain in Figure 4(b) with $\Delta z = 10.0\ m$ and $k_0 = k_{0,min}$. We use a very high cohesion in the entire domain, making the system behave elastically, except at the top layer; there $c_h = 0.1\ MPa$ at $S_s = 0$, and $c_h = 0.3\ MPa$ at $S_s = 1$. We then evaluate the geomechanical stability of the relatively weak top layer during production, while all other layers behave elastically. The friction and dilation angles are $\Psi_f = \pi/6$ and $\Psi_d = 0.0$, respectively. The mass production and thermal injection rates are $Q_p = 0.1\ kg\ s^{-1}$ and $2.0 \times 10^4\ W$, respectively, and gravitational effects are considered.

In Figure 11(a), there is a significant difference in the aqueous phase pressure between the THF predictions based on the 1W and 2W coupling methods. Compaction induced by fluid production causes a high pressure buildup at early times. The two different coupling methods exhibit different evolution paths of the effective stresses during the simulation. As shown in Figure 11(b), the 2W-associated solution enters the plastic regime at an earlier time (i.e., at $t_d \approx 1.7 \times 10^{-3}$, when $\sigma'_m \approx 0.13\ MPa$) than the solution from the 1W formulation does (occurring at $t_d \approx 3.4 \times 10^{-3}$, when $\sigma'_m \approx 0.68\ MPa$). Note the curved line between $\sigma'_m \approx 0.0 \sim 0.435\ MPa$ and $\tau'_m \approx 0.0 \sim\ 0.36\ MPa$ when using the 2W coupling, while the 1W coupling yields a nearly straight or much less curved line. This feature can also be seen in Figures 6 (d) and 8 (d). Thus, the 2W coupling method can detect the danger of failure in weak geological media much earlier and more accurately than the 1W coupling method can, which fails to capture the danger of such an event even when the failure is in progress.

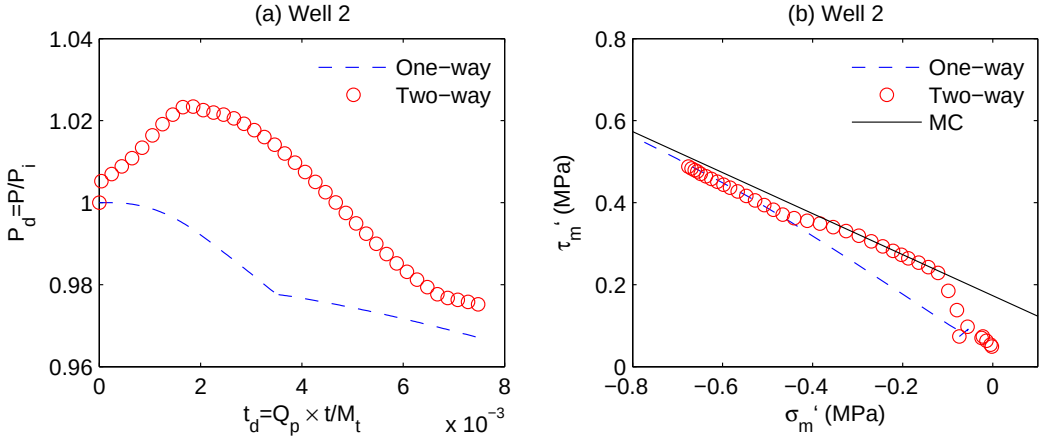

Figure 11: Geomechanical stability of the weak top layer where $c_h = 0.1\ MPa$ at $S_s = 0$ and $c_h = 0.3\ MPa$ at $S_s = 1$. The other layers behave elastically. (a): evolution of the aqueous phase pressure at Well 2; (b) propagation of the effective stresses. Note the significant differences between the THF solutions with the 1W and 2W couplings.

Three-dimensional test problem. Investigating a more realistic problem, we study the coupled processes of fluid flow, heat transport and geomechanics in a three dimensional hydrate deposit in a simulation that accounts for gravity, body force, and

elasticity. In addition to the hydrate-bearing strata, the simulation domain includes other important geological bounding formations: the overburden, the underburden, and side burdens (Figure 12 (a)). Because of symmetry, we only consider a quarter of the domain, which comprises a total of $23 \times 23 \times 16$ grid blocks in (x, y, z) – see Figure 12 (b). The hydrate-bearing stratum involves $20 \times 20 \times 10$ grid blocks in (x, y, z), and the remaining gridblocks in each direction describe the corresponding bounding formations. The space discretization is based on uniform-sized gridblocks with dimensions $\Delta x = 10\ m$, $\Delta y = 10\ m$, and $\Delta z = 10\ m$.

The geomechanical boundary conditions involve an overburden-related total stress of $-9.41\ MPa$ at the top of the domain, zero-vertical displacements at the bottom and zero-horizontal displacements along the sides of the domain. The hydrate-bearing formation is surrounded by no-flow boundaries on all sides. The initial pressure distribution follows the hydrostatic gradient, with $P_i = 9.7\ MPa$ at the top layer. The remaining initial conditions and related properties are uniformly distributed in the deposit, and are as follows: $T_i = 12.5^oC$, $\phi_0 = 0.3$, $S_A = 0.5$, $S_H = 0.5$ and $b = 1.0$. Reservoir fluids are produced from a single vertical well at the center of the system (see Figure 12 (a)) at a mass rate $Q_p = 5.0 \times 10^{-2}\ kg\ s^{-1}$ with no wellbore heating. We assume that the zones outside the hydrate zone are highly permeable, and then the coupled problem outside the hydrate reservoir converges to the representation of the geomechanics problem with drained moduli. In this study, we consider two cases with different intrinsic permeabilities and elastic moduli.

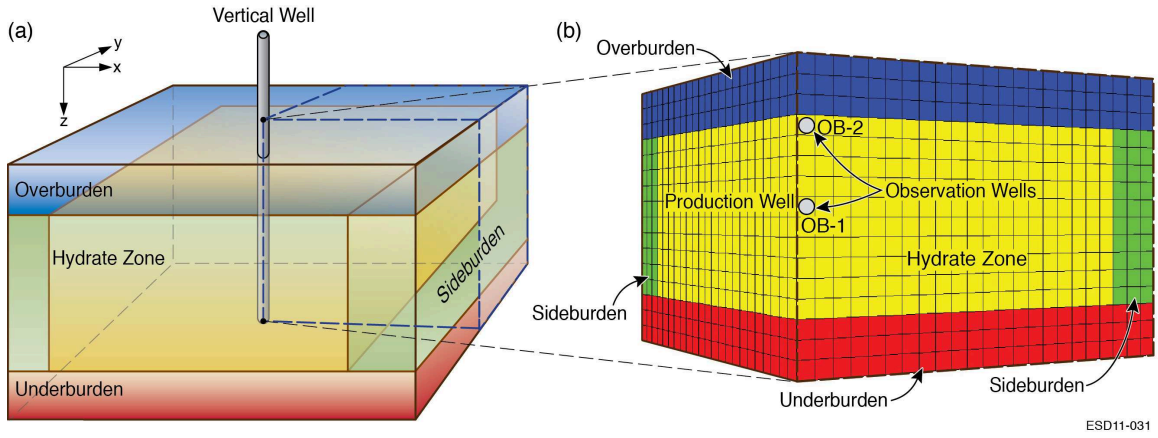

Figure 12: 3D problem of depressurization-induced gas production from a hydrate deposit using a single vertical well: (a) overall system description, depicting the overburden, underburden and sideburdens (left), and (b) description of the simulated domain, which represents only a quarter of the system because of symmetry (right). OB-1 and OB-2 denote observation wells.

Determination of the bulk modulus in fluid flow. In this simulation example, the hydrate-bearing layer has a drained bulk modulus $K_{dr}^{3D} = 200\ MPa$ and a shear modulus of $G_{dr} = 300\ MPa$ that apply over the full range of S_H, while all other zones $K_{dr}^{3D} = 2\ MPa$ and $G_{dr} = 3\ MPa$. The intrinsic permeability of the porous medium in the hydrate-bearing zone is $k_0 = 2.96 \times 10^{-16} m^2 (= 0.3md)$. Because of the reasons already discussed in detail in previous sections, the 1W formulation is not used in this and subsequent 3D studies, all of which are based on a 2W coupling in the THF simulator.

When using 2W coupling, it is possible to choose different bulk moduli for the rock compressibility (Equation 23) in the description of the flow problem, e.g., the constrained modulus K_{dr}^{C} instead of the 3D drained bulk modulus K_{dr}^{3D} (Equation 26), when the reservoir is horizontally constrained.

For simple boundary conditions of linear elastic mechanics, we can obtain the true (exact) local bulk modulus K_{dr}^{t} for the estimation of the rock compressibility in the flow problem. For example, $K_{dr}^{t} = K_{dr}^{C}$ for the Terzaghi problem (Wang, 2000), or $K_{dr}^{t} = K_{dr}^{3D}$ for a fully unconstrained boundary of linear elastic mechanics. However, the true bulk modulus for the rock compressibility cannot be obtained because of heterogeneity, complex mechanical boundary conditions in two or three dimensions, or because of material non-linearity in mechanics. According to the mathematical analysis in Kim et al. (2011d), a less stiff bulk modulus is appropriate to attain numerical stability and convergence. Based the a-priori stability and convergence estimates, the constrained modulus K_{dr}^{C} is not an appropriate choice because it is always stiffer than the true bulk modulus, and it may cause non-convergence or numerical instability (Kim et al., 2011d). In such cases, the approach recommended by Kim et al. (2011d) provides a less-stiff estimate of the bulk modulus for a given dimension (e.g., K_{dr}^{3D} for 3D problems). In Kim et al. (2011d), a 2D consolidation problem is used to support the a-priori stability and convergence estimates. In what follows, we confirm that the mathematical analysis in Kim et al. (2011d) is also supported by full 3D problems.

Figure 13 shows the evolution of pressure at two observation points (OB-1 and OB-2) in the domain when the constrained modulus $K_{dr}^{C} = 600\ MPa$ and the 3D drained bulk modulus $K_{dr}^{3D} = 200\ MPa$ are used in the estimation of rock compressibility. Note that the constrained modulus K_{dr}^{C} is stiffer than the true modulus K_{dr}^{t}, whereas the 3D drained bulk modulus K_{dr}^{C} is less stiff than the true modulus K_{dr}^{t}. As is evident from Figure 13, severe oscillation and near non-convergence occur when we use the constrained bulk modulus. More importantly, according to the a-priori estimates (Kim et al., 2011d), this non-convergence cannot be fixed by reducing time step size, nor disappear for high permeability. Independence from time step

size is surprising because most researchers believe that reducing time step size could fix numerical non-convergence. On the other hand, the THF solutions based on the 3D drained bulk modulus yield monotonic and convergent pressures.

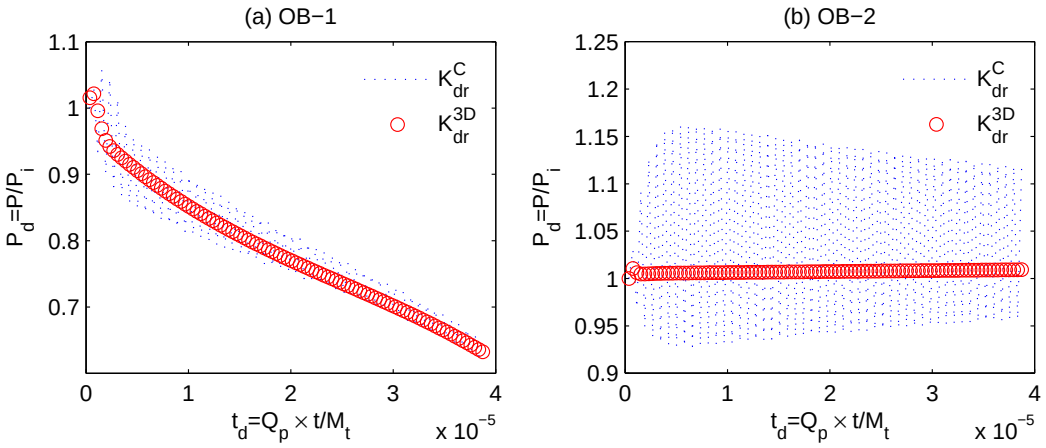

Figure 13: Pressure evolution at (a) OB-1 and (b) OB-2. Use of the constrained modulus $K_{dr}^{C} = 600\ MPa$ with 2W coupling in the flow problem causes severe oscillations and near non-convergence. The less stiff 3D drained bulk modulus $K_{dr}^{3D} = 200\ MPa$ results in stable and convergent solutions.

Mass production with high permeability and stiff surroundings. We repeated the 3D simulation using the same domain, initial and boundary conditions, and system properties, but with a larger $k_0 = 2.96 \times 10^{-14} m^2 (= 30\ md)$. The values of the drained bulk K_{dr}^{3D} and shear G_{dr} moduli for each zone used in the THF simulation are listed in Table 1. The higher k_0 yields fast pressure diffusion at locations OB-1 and OB-2, as shown in Figure 14. The pressure decreases initially very rapidly at OB-1 (which is the production point) while hydrates dissociate – see Figure 14(a). After hydrates completely dissociate at this gridblock (an event which occurs at $t_d \approx 6.83 \times 10^{-4}$), the pressure increases because of an increase in permeability in the hydrate-free medium, and finally appears to stabilize when there is balance between production and fluid release (replacement) from hydrate dissociation. Given the constant Q_p production, a further pressure decline is inevitable at longer times. The evolution of pressure at location OB-2 – see Figure 14(b)– indicates a monotonic pressure decline, and indicates that hydrates have not completely dissociated at the corresponding gridblock. Here, we obtain the stable and monotonic solutions when K_{dr}^{C} is used for the estimation of the rock compressibility in the flow problem. We also observe the stable and monotonic solutions for low permeability $k_0 = 2.96 \times 10^{-16} m^2 (= 0.3\ md)$ (not shown in this paper). The reason for the stable and monotonic solutions is that the drained bulk modulus of the side burden area ($K_{dr}^{3D} = 300 MPa$) is much stiffer than that in the previous case ($K_{dr}^{3D} = 2MPa$). The hydrate zone is more constrained horizontally than that in the previous case, thus the constrained modulus K_{dr}^{C} for the rock compressibility within the hydrate zone is much close to the local true bulk modulus K_{dr}^{t}.

In the previous case, when we use $K_{dr}^{3D} = 20GPa$ for the drained bulk modulus of the side burden area instead of $K_{dr}^{3D} = 2MPa$, we observe that the solutions are stable and monotonic (not shown in this paper), because K_{dr}^{C} in the hydrate zone is close to K_{dr}^{t}. All these numerical behaviors including the earlier simulation 3D results are the unique characteristics in coupled flow and geomechanics, and we find that the mathematical analysis and discussion in Kim et al. (2011d) are also supported by these 3D hydrate reservoir simulations.

Figure 15 shows distributions of the pressure, hydrate saturation S_H, total volumetric strain ε_v, and L_2 norm of the deviatoric strain $\mathbf{e}$, where $\mathbf{e} = \boldsymbol{\varepsilon} - \frac{1}{3}\varepsilon_v \mathbf{1}$, along the diagonal plane of the reservoir domain at the end of simulation, i.e., at $t_d = 7.6 \times 10^{-3}$. As expected, due to depressurization, hydrates dissociate and compaction occurs around the production well (Well 1). As a result, the compaction around the production well causes a relatively large area of shear deformation (Figure 15 (d)), compared with the area of compaction (Figure 15 (c)). Then, the shear deformation may trigger shear failure and geological instability for weak cohesive frictional materials.

Table 1: Drained moduli at each zone of the reservoir domain.

Elastic moduli	Overburden	Side burden	Underburden	Hydrate zone
K_{dr}^{3D}	20 MPa	300 MPa	2 GPa	100 MPa at $S_H = 0.0$, 400 MPa at $S_H = 1.0$
G_{dr}	30 MPa	450 MPa	3 GPa	150 MPa at $S_H = 0.0$, 600 MPa at $S_H = 1.0$

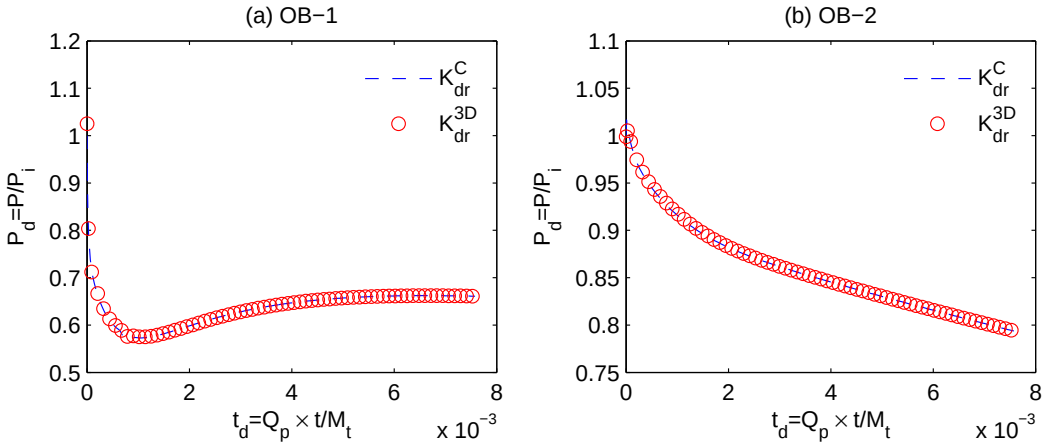

Figure 14: Evolution at the pressure at OB-1 (a) and OB-2 (b). Due to the high permeability, the water pressure diffuses fast. At OB-1, the pressure drops at early time until the hydrate saturation becomes non-zero. After the hydrates completely dissociate at OB-1, the pressure increases and then stabilizes.

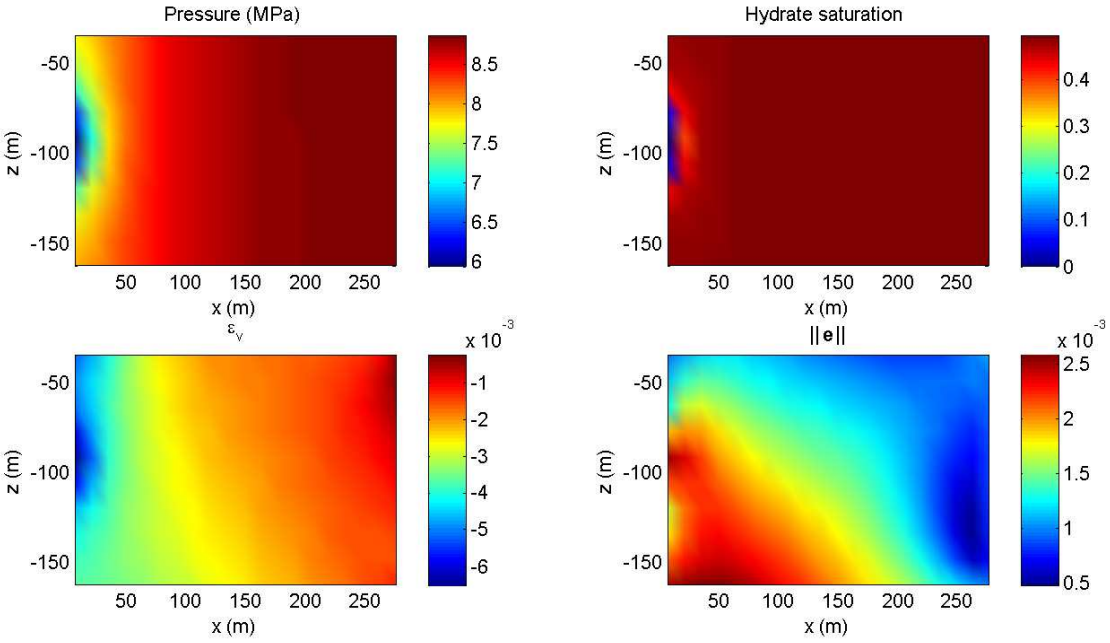

Figure 15: Distributions of the pressure (a), hydrate saturation S_H (b), total volumetric strain ε_v (c), and L_2 norm of the deviatoric strain $\mathbf{e}$ (d), along the diagonal plane of the reservoir domain. Note the hydrate dissociation around the well because of depressurization. Large shear deformation may induce shear failure and geological instability for weak cohesive frictional materials.

Summary and Conclusions.

We have developed, verified, and demonstrated the use of a tightly coupled sequential approach for modeling hydrate reservoirs involving the TOUGH+HYDRATE simulator (Moridis et al., 2008) and the FLAC3D (Itasca, 2006) commercial code. We employed the fixed-stress split method for two-way (2W) coupling as a sequential method that provide numerically stable and convergent solutions. The computational effort of 2W coupling is almost the same as that of one-way (1W) coupling. Two-way coupling method used in this study provides a rigorous 2W coupled simulator that can readily be applied to large scale problems related to processes in hydrate-bearing sediments.

In several test cases involving depressurization, thermal loading, and plasticity we found noticeable differences in the simulation results between 1W and 2W coupling methods. The differences are due to the following factors: (i) hydrate reservoirs typically have a high coupling strength, because the solid skeleton becomes soft during the dissociation of hydrates and water is highly incompressible, although gas is compressible; (ii) fluid flow and geomechanics processes occur on different time scales; because the mechanics response is quasi-static, the perturbation by fluid production or injection is propagated instantaneously and affects the flow (hydraulic) parameters and properties; and (iii) the existence of the solid phases (i.e., hydrate and ice) leads to low permeability, even though the intrinsic permeability is high. For early times or a low permeability system, the effects resulting from the different time scales of fluid flow and geomechanics can become large. We also confirm that full 3D simulations for hydrate reservoirs support the a-priori numerical stability and convergence estimates in Kim et al. (2011d).

Acknowledgements.

We are grateful for the editorial review by Dan Hawkes and the graphic design by Diana Swantek at the Lawrence Berkeley National Laboratory. This work was supported by the Assistant Secretary for Fossil Energy, Office of Natural Gas and Petroleum Technology, through the National Energy Technology Laboratory, under the U.S. Department of Energy, Contract No. DE-AC02-05CH11231.

Nomenclature.

$\mathbf{C}_{dr}$ Drained-isothermal elasticity tensor

C Skeleton volumetric heat capacity

C_d Total volumetric heat capacity

$C_{p,J}$ Volumetric specific heat capacity at constant pressure for the phase J

C_R Heat capacity of the porous media

$\mathbf{D}_J^\kappa$ Hydrodynamic dispersion tensor

E Young's modulus

K_{dr} Drained isothermal bulk modulus

K_{dr}^e, K_{dr}^{ep} Elastic and elastoplastic bulk moduli

K_{dr}^C Constrained modulus

K_{dr}^{3D} 3D drained bulk modulus

K_{dr}^t True (exact) local bulk modulus K_{dr}^t

K_s Intrinsic solid grain bulk modulus

$\mathbf{J}_J^k$ Diffusive mass flux of the component k in the phase J

M_t Total initial mass in place

$\mathbf{M} = \{M_{JK}\}$ Biot modulus matrix

N_H Hydration number

$\mathbf{N} = \{N_{JK}\}$ Inverse matrix of the Biot modulus matrix

Q_H Specific enthalpy of hydrate formation/dissociation

Q_h Enthalpy injection

Q_p Total mass production rate

$\bar{S}$ Total entropy

S_J Saturation of the phase J

T Temperature

W^k Molecular weight of the component k

X_J^k Mass fraction of the component k in the phase J

b Biot coefficient in single phase flow

b_J Biot coefficient for of the phase J

c_h Cohesion for the Mohr-Coulomb failure criterion

c_J Compressibility of the fluid phase J

c_p Pore compressibility

c_v Consolidation coefficient

$\mathbf{e}$ Deviatoric strain

e_J Specific internal energy of the phase J

$\mathbf{f}^\theta$ Flux of the heat

f**,** g Yield criterion and the plastic potential function

$\boldsymbol{g}$ Gravity vector

k_K Klinkenberg factor

$\mathbf{k}$ Absolute permeability tensor

k_{rJ} Relative permeability for the fluid phase J

$k_{\theta w}$**,** $k_{\theta d}$ Wet and dry thermal conductivities, respectively

m_H^w**,** m_H^m Pseudostorage terms for the hydrate

m^k Mass of component k

m^θ Accumulation of the heat

P_{co} **(**P_c**)** Capillary pressure between oil and water

P_E Equivalent pore-pressure

P_J Pressure for the fluid phase J

q^k Source of mass of the component k

s_J Specific entropy

q^θ Source of the heat

$\boldsymbol{t}$ Traction

$\boldsymbol{u}$ Displacement

$\mathbf{w}_J^k$ Convective mass flux of the component k in the phase J

Δx Grid spacing in the x axis

Δy Grid spacing in the y axis

Δz Grid spacing in the z axis

$\Delta\Phi$ Porosity correction

Φ Lagrange's porosity

Φ_c Critical porosity

Ψ_f, Ψ_d Friction and dilation angles for the Mohr-Coulomb failure criterion

$3\alpha_T$ Volumetric skeleton thermal dilation coefficient

$3\alpha_\phi$, $3\alpha_J$ Coefficients of thermal dilation related to porosity and the phase J

$\boldsymbol{\varepsilon}$ Linearized total strain tensor

ε_v Total volumetric strain

$\varepsilon_{v,e}$, $\varepsilon_{v,p}$ Elastic and plastic volumetric strains

γ_1, γ_2 Coefficients for permeability

μ_J Viscosity for the fluid phase J

ν Poisson's ratio

ϕ True porosity, Euler's porosity

ρ_b Bulk density

ρ_J Density of the phase J

ρ_R Density of the porous media

$\boldsymbol{\sigma}$ Cauchy total-stress tensor

$\boldsymbol{\sigma}'$ Effective stress tensor

σ'_1, σ'_2, σ'_3 Maximum, intermediate, and minimum principal effective stresses

τ_g Gas tortuosity

$\mathbf{f}^k$ Flux of mass of the component k

$(\cdot)^\theta$ Heat component

$(\cdot)_0$ Reference state

$(\cdot)_d$ Dimensionless quantity

$(\cdot)^n$ Time level

$\dot{(\,)}$ Time derivative

$\mathbf{Grad}$ Gradient operator

Div Divergence operator

$\mathbf{1}$ Rank-2 identity tensor

References

Abousleiman A., Cheng A., Detournay E., and Roegiers J. 1996. Mandel's problem revisited. *Geotechnique* **46**: 187–195.

Armero F. 1999. Formulation and finite element implementation of a multiplicative model of coupled poro-plasticity at finite strains under fully saturated conditions. *Comput. Methods Appl. Mech. Engrg.* **171**: 205–241.

Armero F. and Simo J.C. 1992. A new unconditionally stable fractional step method for non-linear coupled thermomechanical problems. *Int. J. Numer. Meth. Engrg.* **35**: 737–766.

Bagheri M. and Settari A. 2008. Modeling of Geomechanics in Naturally Fractured Reservoirs. *SPE Reserv. Eval. Eng.* **11**(1): 108–118.

Biot M.A. 1941. General theory of three-dimensional consolidation. *J. Appl. Phys.* **12**: 155–164.

Borja R.I., Sama K.M., and Sanz P.F. 2003. On the Numerical Integration of Three-invariant Elastoplastic Constitutive Models. *Comput. Methods Appl. Mech. Engrg.* **192**: 1227–1258.

Coussy O. 1995. *Mechanics of porous continua*. Chichester, England: John Wiley and Sons.

Coussy O. 2004. *Poromechanics*. Chichester, England: John Wiley and Sons.

Coussy O., Eymard R., and Lassabatére T. 1998. Constitutive modeling of unsaturated drying deformable materials. *J. Eng. Mech.* 658–557.

Dean R.H., Gai S., Stone C.M., and Minkoff S.E. 2006. A comparison of techniques for coupling porous flow and geomechanics. *Soc. Pet. Eng. J.* **11**(1): 132–140.

Felippa C.A. and Park K.C. 1980. Staggered transient analysis procedures for coupled mechanical systems: formulation. *Comput. Methods Appl. Mech. Engrg.* **24**: 61–111.

Freeman T.T., Chalaturnyk R.J., and Bogdanov I.I. 2009. Geomechanics of heterogeneous bitumen carbonates. SPE Res Simul Sym (SPE 119151), Woodland TX, 2-4 Feb.

Gai X. 2004. A coupled geomechanics and reservoir flow model on parallel computers. Ph.D. Dissertation, University of Texas at Austin.

Hughes T.J.R. 1987. *The Finite Element Method: Linear Static and Dynamic Finite Element Analysis*. Englewood Cliffs, NJ: Prentice-Hall.

Itasca 2006. FLAC3D (Fast Lagrangian Analysis of Continua in 3 Dimensions), Version 3.1. Minneapolis, Minnesota, itasca Consulting Group.

Jean L., Mainguy M., Masson R., and Vidal-Gilbert S. 2007. Accelerating the convergence of coupled geomechanical-reservoir simulations. *Int. J. Numer. Anal. Methods Geomech.* **31**: 1163–1181.

Jha B. and Juanes R. 2007. A locally conservative finite element framework for the simulation of coupled flow and reservoir geomechanics. *Acta Geotechnica* **2**: 139–153.

Kim J., Tchelepi H.A., and Juanes R. 2011a. Rigorous Coupling of Geomechanics and Multiphase Flow with Strong Capillarity. SPE Res Simul Sym (SPE 141268), Woodland, 21-23 Feb.

Kim J., Tchelepi H.A., and Juanes R. 2011b. Stability, Accuracy, and Efficiency of Sequential Methods for Coupled Flow and Geomechanics. *Soc. Pet. Eng. J.* **16**(2): 249 – 262. Doi:10.2118/119084-PA.

Kim J., Tchelepi H.A., and Juanes R. 2011c. Stability and convergence of sequential methods for coupled flow and geomechanics: Drained and undrained splits. *Comput. Methods Appl. Mech. Engrg.* **200**: 2094–2116.

Kim J., Tchelepi H.A., and Juanes R. 2011d. Stability and convergence of sequential methods for coupled flow and geomechanics: Fixed-stress and fixed-strain splits. *Comput. Methods Appl. Mech. Engrg.* **200**: 1591–1606.

Kosloff D., Scott R., and Scranton J. 1980. Finite element simulation of Wilmington oil field subsidence: I. linear modelling. *Tectonophysics* **65**: 339–368.

Kowalsky M.B. and Moridis G.J. 2007. Comparison of Kinetic and Equilibrium Reaction Models in Simulating the Behavior of Gas Hydrates in Porous Media. *J. Energy Conv. Mgmt.* **48**(6): 1850–1863 (doi: 10.1016/j.enconman.2007.01.017).

Lewis R.W. and Schrefler B.A. 1998. *The finite element method in the static and dynamic deformation and consolidation of porous media*. Chichester, England: Wiley, 2nd edition.

Makogon M. 1987. Gas hydrates: frozen energy. *Recherche* **18**(192): 1192.

Makogon Y. 1997. *Hydrates of Hydrocarbons*. Tulsa, OK: Penn Well Publishing Co.

Merle H.A., Kentie C.J.P., van Opstal G.H.C., and Schneider G.M.G. 1976. The Bachaquero Study - A composite analysis of the behavior of a compaction drive/solution gas drive reservoir. *J. Pet. Technol.* 1107–1114.

Millington R.J. and Quirk J.P. 1961. Permeability of Porous Solids. *Trans. Faraday Soc.* **57**: 1200–1207.

Moridis G.J. 2003. Numerical studies of gas production from methane hydrates. *Soc. Pet. Eng. J.* **8**(4): 359–370.

Moridis G.J., Collett T.S., Boswell R., Kurihara M., Reagan M.T., Koh C., and Sloan E.D. 2009a. Toward Production From Gas Hydrates: Current Status, Assessment of Resources, and Simulation-Based Evaluation of Technology and Potential. *SPE Reserv. Eval. Eng.* **12**(5): 745–771 (doi: 10.2118/114163–PA).

Moridis G.J., Collett T.S., Pooladi-Darvish M., Hancock S., Santamarina C., Boswell R., Kneafsey T., Rutqvist J., Kowalsky M., Reagan M.T., Sloan E.D., Sum A.K., and Koh C. 2011. Challenges, Uncertainties and Issues Facing Gas Production From Gas Hydrate Deposits. *SPE Reserv. Eval. Eng.* **14**(1): 76–112 (doi: 10.2118/131792–PA).

Moridis G.J., Kowalsky M.B., and Pruess K. 2008. TOUGH+HYDRATE v1.0 User's Manual: A Code for the Simulation of System Behavior in Hydrate-Bearing Geologic Media. Report LBNL-00149E, Lawrence Berkeley National Laboratory, Berkeley, CA.

Moridis G.J., Seol Y., and Kneafsey T. 2005. Studies of Reaction Kinetics of Methane Hydrate Dissociation in Porous Media. The 5th International Conference on Gas Hydrates, Trondheim, Norway, lBNL-57298.

Murad M.A. and Loula A.F.D. 1992. Improved accuracy in finite element analysis of Biot's consolidation problem. *Comput. Methods Appl. Mech. Engrg.* **95**: 359–382.

Murad M.A. and Loula A.F.D. 1994. On stability and convergence of finite element approximations of Biot's consolidation problem. *Comput. Methods Appl. Mech. Engrg.* **37**: 645–667.

Phillips P.J. and Wheeler M.F. 2007a. A coupling of mixed and continuous Galerkin finite element methods for poroelasticity I: the continuous in time case. *Comput. Geosci.* **11**: 131–144.

Phillips P.J. and Wheeler M.F. 2007b. A coupling of mixed and continuous Galerkin finite element methods for poroelasticity II: the discrete-in-time case. *Comput. Geosci.* **11**: 145–158.

Rutqvist J. and Moridis G.J. 2009. Numerical Studies on the Geomechanical Stability of Hydrate-Bearing Sediments. *Soc. Pet. Eng. J.* **14**(2): 267–282.

Rutqvist J., Moridis G.J., Grover T., and Collett T. 2009. Geomechanical Response of Permafrost-Associated Hydrate Deposits to Depressurization-Induced Gas Production. *J. Pet. Sci. Eng.* **67**: 1–12.

Rutqvist J., Moridis G.J., and Reagan M. 2010a. Geomechanical Response of Sloping Oceanic Hydrate Deposits to Thermal Loading and Production Activities. 2010 Offshore Technology Conference (OTC 21048), Houston TX, 3-6 May.

Rutqvist J., Vasco D., , and Myer L. 2010b. Coupled reservoir-geomechanical analysis of CO2 injection and ground deformations at In Salah, Algeria. *Int. J. Greenhouse Gas Control* **4**: 225 – 230.

Settari A. and Mourits F. 1998. A coupled reservoir and geomechanical simulation system. *Soc. Pet. Eng. J.* **3**: 219–226.

Sloan E. and Koh C. 2008. *Clathrate Hydrates of Natural Gases*. New York, New York: CRC Press, Taylor and Francis Group, Publishers, 3rd edition.

Tran D., Settari A., and Nghiem L. 2004. New iterative coupling between a reservoir simulator and a geomechanics module. *Soc. Pet. Eng. J.* **9**(3): 362–369.

Vermeer P.A. and Verruijt A. 1981. An accuracy condition for consolidation by finite elements. *Int. J. Numer. Anal. Methods Geomech.* **5**: 1–14.

Wan J. 2002. Stabilized finite element methods for coupled geomechanics and multiphase flow. Ph.D. Dissertation, Stanford University.

Wang H.F. 2000. *Theory of Linear Poroelasticity*. Princeton University Press.

Wang X., Wang L.B., and Xu L.M. 2004. Formulation of the return mapping algorithm for elastoplastic soil models. *Comput. Geotech.* **31**: 315–338.

White A.J. and Borja R.I. 2008. Stabilized low-order finite elements for coupled solid-deformation/fluid-diffusion and their application to fault zone transients. *Comput. Methods Appl. Mech. Engrg.* **197**: 43534366.

Zienkiewicz O.C., Paul D.K., and Chan A.H.C. 1988. Unconditionally stable staggered solution procedure for soil-pore fluid interaction problems. *Int. J. Numer. Meth. Engrg.* **26**(5): 1039–1055.